PHYSICAL REVIEW C VOLUME 47, NUMBER 4 APRIL 1993

Coplanar and noncoplanar *pp* bremsstrahlung

A. Katsogiannis and K. Amos

School of Physics, University of Melbourne, Parkville, Victoria 3052, Australia

(Received 12 August 1992)

The Harvard noncoplanar geometry is used to specify calculations of the differential and integrated cross sections and of the component analyzing powers from *pp* bremsstrahlung. This geometry is equivalent to spherical polar coordinates for coplanar scattering. A wide range of incident energies and symmetric proton emission angles are considered in studying various properties of the reaction. Emphasis is placed on an energy of 280 MeV and for forward proton angles, at which results are most sensitive to specific off-of-the-energy-shell properties of the two nucleon t matrices. Those t matrices are generated with various interactions. The importance of the NN t-matrix off-diagonal tensor contributions for the coplanar observables as demonstrated in the pioneering work of Brown is clearly shown. Photon cross sections vary with the noncoplanarity of the reaction due in part to changes in relative importance of diverse NN channel t matrices. The analyzing powers likewise vary with azimuthal angle and reveal a particular sensitivity to the tensor coupled $^3P_2$-$^3F_2$ channels and to the $^3P_0$ channel.

PACS number(s): 13.75.Cs, 21.30.+y

I. INTRODUCTION

The *pp*-bremsstrahlung ($pp\gamma$) reaction is the most unambiguous reaction from which to obtain off-shell information of the NN force. This is the case because the electromagnetic interaction is not only weak relative to the strong force but also well understood. The reaction is also the simplest process in which off-shell effects increase with energy and complications can be avoided by working with energies only above which other processes become important (such as the pion threshold). Consequently, there was much interest in the reaction in the 1960s and 1970s but no major inroads were made in extracting decisive off-shell information then and interest later waned. More recently there has been a renewed interest due primarily to higher precision and sophistication of experiments and of theoretical analyses [1–3]. The recent TRIUMF experiments included the first extensive measurements of the analyzing power. The difficulty in obtaining such measurements (and of other polarization observables) has thwarted progress in the past. Now there are facilities in preparation (COSY in Jülich and TRIUMF) which should produce more precise data. There are also some initial results from the Indiana University Cyclotron Facility (IUCF) Cooler-Ring [4] which look promising.

In view of this activity it seems appropriate to take a closer look at various aspects of the reaction and, given that the recent work thus far has concentrated solely on coplanar events, we extend upon this by studying noncoplanar events. Older calculations [5–7] suggest that the photon cross section, while quite insensitive to polar angle variations in the reference plane, is very sensitive to azimuthal angles. With the new measurements taken at energies close to pion threshold it would be instructive to observe noncoplanar events as even coplanar geometry detectors will accept these events to some extent due to their finite size. Thus, we undertake a general noncoplanar calculation at such energies in order to study the azimuthal behavior of the observables. The noncoplanar analyzing power is calculated for the first time. Furthermore, the behavior of the electric and magnetic contributions to the photon angular distribution, including the known suppression of the convection current, are shown explicitly with increasing energy. The electric suppression as a function of the azimuthal angle, suggested by Drechsel and Maximon [5], will also be displayed.

The noncoplanar observables reflect the off-shell behavior of the NN t matrices and we study that in some detail. The noncoplanar kinematics reveal a steadily increasing photon momentum with increasing noncoplanarity which suggests a stronger dependence upon off-shell properties of the NN t matrices. This, it was hoped, would be reflected in the observables, particularly the analyzing power. Additionally, for noncoplanar geometries, the x and z components of the analyzing power are no longer trivial and may provide further useful information. In order to enhance off-shell effects, the most sensitive off-shell region was scrutinized, namely, forward proton scattering near pion threshold.

Our calculation follows along similar lines to the TRIUMF work of Workman and Fearing [1]. Included are relativistic spin corrections (RSC), one-pion-exchange (OPE) amplitudes, and off-shell Coulomb corrections; the latter will be discussed in detail in a later paper. Rescattering terms have been omitted in the current work but as the calculations have been made using the center-of-momentum frame, the leading term of the rescattering vanishes identically. The effects of the RSC close to pion threshold will be discussed in the coplanar geometry, for which they are most important. We also briefly look at the effect upon results of partial wave cutoffs near pion threshold.

For our noncoplanar calculations the Harvard noncoplanar geometry [6] was chosen as with this geometry the observables are more conveniently scanned, over the whole range of photon angles, 0° to 360°. Increasing noncoplanarity restricts the photon polar angles towards the "limiting photon." The variables can quite readily be transformed to spherical polar coordinates.

The Lippmann-Schwinger equation is solved to specify the NN t matrices. Four interactions were used: the Paris [8], the Bonn OBEPQ [9], the extended Reid soft core [10], and a phenomenological interaction developed some time ago in Melbourne [11]. The latter force was designed to fit on-shell Arndt [12] phase shifts in all channels with momentum-dependent functions. The effective tensor force of this interaction is much weaker than those of the other forces, whence comparisons can contrast and emphasize effects of the "realistic" tensor channels.

In Sec. II we detail our method of calculation for the kinematics and in Sec. III we discuss some important properties of the T matrix and consequently give the details of its calculation. Other contributions and their significance in $pp\gamma$ are discussed in Sec. IV. The frame transformations and the calculation of our observables are given in Secs. V and VI, respectively. Our results are presented and discussed in Sec. VII and conclusions are drawn in Sec. VIII.

II. KINEMATICS

As a discussion on the kinematics for bremsstrahlung has not been included in recent papers we do so in some detail here, including the solution for noncoplanar events. All kinematics have been done relativistically and without approximation, unlike in the older presentation of Drechsel and Maximon [5], and so are valid for coplanar and noncoplanar events at all energies. The Harvard noncoplanar geometry as specified by Liou and Sobel [6] is utilized as the coordinate system defining the incoming and outgoing momenta. This has several advantages over conventional spherical polar coordinates. Notably, the restricted emission angles for noncoplanar scattering in the spherical polar geometry can be avoided. The geometry used is shown in Fig. 1, wherein it is to be noted that the azimuthal and polar angles are defined relative

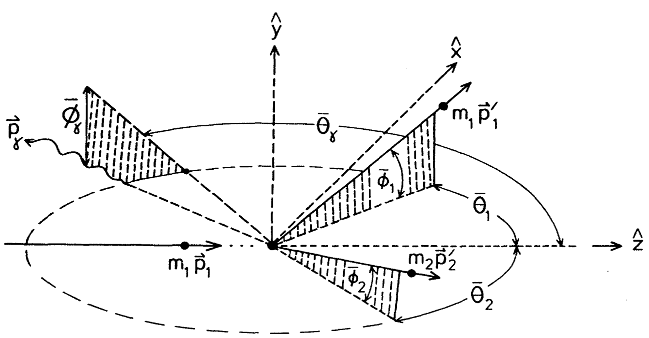

FIG. 1. Kinematics for bremsstrahlung in the Harvard noncoplanar geometry.

to the reference x-z plane so distinguishing these coordinates, $(\bar{\theta}_1, \bar{\phi}_1, \bar{\theta}_2, \bar{\phi}_2, \bar{\theta}_\gamma, \bar{\phi}_\gamma)$, from the spherical polar angle set $(\theta_1, \phi_1, \theta_2, \phi_2, \theta_\gamma, \phi_\gamma)$. The low energy proton (LEP), which is on the same side of the y-z plane as the photon emission, is taken to be proton 1 along the positive x axis. Due to symmetry we need only consider proton 1 momenta along the positive x axis. The Harvard noncoplanar geometry is equivalent to spherical polar coordinates for coplanar events and is also instructive for noncoplanar events as the proton energies are always far greater than the photon energy. Thus, via energy-momentum conservation, scattering of the protons can only be made slightly out of the reference x-z plane. These coordinates are easily related to spherical polar coordinates [6] and, for noncoplanar events, the phase space factor for the photon angular distribution is finite for all photon emissions. The phase space factor in spherical polars diverges at the extreme photon emission angles for noncoplanar scattering.

Nine variables are to be determined with energy-momentum conservation providing four constraints upon them. For the remaining five independent variables the set $(\bar{\theta}_1, \bar{\phi}_1, \bar{\theta}_2, \bar{\phi}_2, \psi_\gamma)$ is chosen. The photon angle ψ_γ is defined below and subsequently we seek observables for $pp\gamma$ in terms of these variables, such as the photon cross section,

$$\frac{d^5\sigma}{d\bar{\theta}_1 d\bar{\phi}_1 d\bar{\theta}_2 d\bar{\phi}_2 d\psi_\gamma} = \frac{d^3\sigma}{d\Omega_1' d\Omega_2' d\psi_\gamma} , \tag{1}$$

and the components of the analyzing power, A_x, A_y, and A_z.

A. Definition of ψ_γ

Energy-momentum conservation determines a limiting maximum angle out of the x-z plane for the symmetric azimuthal proton angle given by

$$\bar{\phi} = \frac{(\bar{\phi}_1 + \bar{\phi}_2)}{2} , \tag{2}$$

i.e., $\bar{\phi} = \bar{\phi}_{\mathrm{max}}$, corresponding to a "limiting γ ray" with the photon angle set $(\bar{\theta}_0, \bar{\phi}_0)$.

If the "limiting photon" momentum is defined by $\mathbf{k_0}$ then a new photon momentum can be defined as [13]

$$\mathbf{k}' = \mathbf{k} - \alpha \mathbf{k_0} , \tag{3}$$

with α chosen such that $\mathbf{k}'$ always lies in the reference plane. Then, ψ_γ is specified as the polar angle of $\mathbf{k}'$ and spans the range 0–2π rad. It is related to the photon polar and azimuthal angles [6] via

$$\tan \psi_\gamma = \frac{\tan \bar{\phi}_0 \sin \bar{\theta}_\gamma - \sin \bar{\theta}_0 \tan \bar{\phi}_\gamma}{\tan \bar{\phi}_0 \cos \bar{\theta}_\gamma - \cos \bar{\theta}_0 \tan \bar{\phi}_\gamma} . \tag{4}$$

For symmetric cases, $\bar{\theta}_1 = \bar{\theta}_2 = \bar{\theta}$ and $\bar{\phi}_1 = \bar{\phi}_2 = \bar{\phi}$, this becomes

$$\tan\psi_\gamma = \frac{\tan\bar\phi_0 \sin\bar\theta_\gamma}{\tan\bar\phi_0\cos\bar\theta_\gamma - \tan\bar\phi_\gamma}\ , \tag{5}$$

since $\bar\theta_0 = 0$. We are concerned, herein, with symmetric proton angles and the values for $\bar\phi_0$ and $\bar\phi_{\max}$ were sought by using a root-finding process for $\bar\phi_0$.

B. Solution of kinematics

In terms of the variables for the Harvard noncoplanar geometry the energy-momentum conservation equations for the reaction, in the laboratory frame, are

$$p_1'\sin\bar\theta_1\cos\bar\phi_1 - p_2'\sin\bar\theta_2\cos\bar\phi_2 + k\sin\bar\theta_\gamma\cos\bar\phi_\gamma = 0 \quad (x \text{ direction})\ , \tag{6}$$

$$p_1'\sin\bar\phi_1 + p_2'\sin\bar\theta_2 - k\sin\bar\phi_\gamma = 0 \quad (y \text{ direction}), \tag{7}$$

$$p_1'\cos\bar\theta_1\cos\bar\phi_1 - p_2'\cos\bar\theta_2\cos\bar\phi_2 + k\cos\bar\theta_\gamma\cos\bar\phi_\gamma = p_1 \quad (z \text{ direction}), \tag{8}$$

$$E_{\mathbf{p}_1} + E_{\mathbf{p}_2} = E_{\mathbf{p}_1'} + E_{\mathbf{p}_2'} + E_{\mathbf{k}} \quad (\text{energy conservation}), \tag{9}$$

where $E_{\mathbf{p}_1} = \sqrt{(p_1c)^2 + (mc^2)^2}$, $E_{\mathbf{p}_2} = mc^2$, $E_{\mathbf{k}} = kc$, $E_{\mathbf{p}_i'} = \sqrt{(p_i'c)^2 + (mc^2)^2}$, and m is the proton mass. The solutions to the kinematics are obtained by eliminating the five independent kinematic variables analytically from Eqs. (6)–(9) and using a root-finding procedure for the one remaining variable.

The method Liou and Sobel [6] present in the appendix of their paper can be utilized to find the outgoing momenta via matrix inversion of Eqs. (6)–(8). However, in the coplanar geometry, Eq. (7) is trivial and the coefficient matrix obtained for p_1', p_2', and k is singular. The energy equation is nonlinear in these variables and so cannot be substituted in for this purpose.

The coplanar and noncoplanar kinematics are quite distinct problems in our development. For the coplanar case we have $\psi_\gamma = \bar\theta_\gamma = \theta_\gamma$, where θ_γ is the spherical polar photon angle, and three equations for three unknowns remain. From these we obtain a quartic function in the outgoing momentum, p_1'. In the noncoplanar case, on the other hand, there are five unknowns supplemented by five equations: the energy-momentum equations and Eq. (4). The result is a rather complicated function in the chosen (last) variable, which we have chosen to be $\bar\theta_\gamma$. In both cases the roots are easily computed within the allowed range of values for the variables and the physical roots readily extracted.

C. Noncoplanar kinematic behaviour

The kinematic conditions of bremsstrahlung with increasing noncoplanarity, characterized by $\bar\phi$, has a number of features important in the interpretation of results. As this angle increases the protons emerge out of the reference x-z plane in the positive y direction while the photons are emitted out of the plane in the negative y direction. With increasing $\bar\phi$ the massless photons move out of the plane much more rapidly than the protons. The movement out of plane is not symmetric but is slightly tilted forward [5]. Their emission is restricted to greater photon azimuthal angles, $\bar\phi_\gamma$, as they all converge towards the "limiting photon" direction. This limit lies slightly forward of $\bar\phi_0 = 90°$ for $\bar\phi = \bar\phi_{\max}$ and $\bar\phi_{\max}$ depends upon the incident energy and proton polar angles, $\bar\theta_1$ and $\bar\theta_2$. At 280 MeV and proton angles between 5° and 30° its value lies in the range 5°–10°.

As shown in Sec. II A the "limiting photon" momentum can be used to project any photon emission momentum onto the reference plane. Thereby, the restricted angles of emission transform to the angle variable ψ_γ that spans a 0°–360° range, making it particularly useful for theoretical studies. A disadvantage is that results then do not have a simple geometric interpretation. However, if required, the chosen variables can be transformed to spherical polar coordinates.

III. DETAILS AND FEATURES OF THE CALCULATION

A potential model calculation of $pp\gamma$ has been made. Such was undertaken by a number of authors in older calculations [5, 6, 14, 15] and these were reasonably successful at fitting the available data. More recently advances have been made on both theoretical and experimental fronts. New calculations have been reported which are more precise and include many improvements upon the older works. The new calculations fit data taken at higher energies quite successfully and particularly data taken near pion threshold. Also, they are consistent with measurements of spin observables such as the TRIUMF analyzing powers [16–18].

In turn, within the potential model two distinctive approaches may be taken which, in principle, are the same. In the first, solutions to the Schrödinger equation in configuration space are sought and the ensuing wave functions used in calculating the matrix elements of the electomagnetic operator. This approach has been taken by several authors [14, 15]. In the second approach, the transition amplitude is considered in momentum space whereupon it factorizes into a nucleon-nucleon (NN) part, a propagator, and an electromagnetic vertex. This is the most common approach to calculating $pp\gamma$ [1, 2, 5, 6] and we use it also as the factorization most clearly identifies the NN t matrix, in which we have prime interest.

The NN t matrices are solutions of the Lippmann-Schwinger equation, using momentum space representation, which we obtain from matrix inversion. We find that these solutions are very stable, particularly for higher partial waves. The NN interaction is specified without approximation while the weakness of the electromagnetic interaction allows it to be taken only to first order. The most important relativistic corrections (the RSC) have been included.

As the full T-matrix formalism has been developed in some detail [1, 2, 5, 6, 14] only the salient features of that development are given and included are any new aspects and changes required in order to incorporate noncoplanar events.

Beginning with the Gell-Mann and Goldberger two-potential formalism [19] the full T-matrix operator can be written as

$$T = V_{\mathrm{em}} + [t^-(E_f)]^\dagger G^+(E_f)V_{\mathrm{em}} + V_{\mathrm{em}}G^+(E_i)t^+(E_i)$$
$$+[t^-(E_f)]^\dagger G^+(E_f)V_{\mathrm{em}}G^+(E_i)t^+(E_i)\ , \qquad (10)$$

in which the i and f indices refer to initial and final proton states respectively, the (–) and (+) superscripts refer to incoming and outgoing boundary conditions, respectively, and E is the energy of the two protons. The operator $t(E)$ is the NN t matrix, V_{em} is the electromagnetic operator, and $G(E)$ is the propagator for the protons. The V_{em} and NN t-matrix operators do not commute. All the NN t matrices and propagators have outgoing wave boundary conditions. The first term in Eq. (10), the zero scattering term, is forbidden as it represents radiation by a free particle. The next two are the single scattering terms and the fourth is the rescattering term. We ignore the rescattering in the current work.

Expectation values of the full T matrix are formed using the relative proton states $|\mathbf{p}, \mathbf{S}, \mathbf{M}\rangle$ and photon states $|\mathbf{k}\rangle$, where $\mathbf{p}$, S, and M are relative proton momentum, total spin, and spin projection, respectively, and $\mathbf{k}$ is the photon momentum. The spin space matrix element for the full T operator is developed in the center-of-momentum (CM) frame to be

$$\langle S'M'|T|SM\rangle = \sum_{S''M''}\left\{ \frac{\langle S''M'', \frac{1}{2}(\mathbf{p}_1 - \mathbf{p}_2 - \mathbf{k})\,|t^-(E_f)|\,\frac{1}{2}(\mathbf{p}_1' - \mathbf{p}_2'), S'M'\rangle^* \langle S''M''|V_{\mathrm{em}}^{(1)}|SM\rangle}{(E_f - E_{\mathbf{p}_1-\mathbf{k}} - E_{\mathbf{p}_2})} \right.$$
$$+ \frac{\langle S''M'', \frac{1}{2}(\mathbf{p}_1 - \mathbf{p}_2 + \mathbf{k})|t^-(E_f)|\frac{1}{2}(\mathbf{p}_1' - \mathbf{p}_2'), S'M'\rangle^* \langle S''M''|V_{\mathrm{em}}^{(2)}|SM\rangle}{(E_f - E_{\mathbf{p}_1} - E_{\mathbf{p}_2-\mathbf{k}})}$$
$$+ \frac{\langle S'M'|V_{\mathrm{em}}^{(1)'}|S''M''\rangle\langle S''M'', \frac{1}{2}(\mathbf{p}_1' - \mathbf{p}_2' + \mathbf{k})|t^+(E_i)|\frac{1}{2}(\mathbf{p}_1 - \mathbf{p}_2), SM\rangle}{(E_i - E_{\mathbf{p}_1'+\mathbf{k}} - E_{\mathbf{p}_2'})}$$
$$\left. + \frac{\langle S'M'|V_{\mathrm{em}}^{(2)'}|S''M''\rangle\langle S''M'', \frac{1}{2}(\mathbf{p}_1' - \mathbf{p}_2' - \mathbf{k})|t^+(E_i)|\frac{1}{2}(\mathbf{p}_1 - \mathbf{p}_2), SM\rangle}{(E_i - E_{\mathbf{p}_1'} - E_{\mathbf{p}_2'+\mathbf{k}})} \right\}. \qquad (11)$$

The energies are given relativistically, via $E_{\mathbf{p}} = \sqrt{(\mathbf{p}c)^2 + (mc^2)^2}$. The unprimed (primed) $V_{\mathrm{em}}^{(i)\{'\}}$ operator represents proton i in the initial (final) state. In this expression we have used the relation

$$\langle SM, \mathbf{p}|\ [t^-(E_{\mathbf{p}})]^\dagger\ |\mathbf{p}', S'M'\rangle$$
$$= \langle S'M', \mathbf{p}'|t^-(E_{\mathbf{p}})|\mathbf{p}, SM\rangle^*\ . \quad (12)$$

The single scattering contributions are expressed in terms of four algebraic functions. At this point it should be noted that the kinematics, phase space factor, propagators, and full T-matrix formalism are derived within a relativistic framework. However, the electromagnetic and NN interactions are both given nonrelativistically as are their corresponding matrix elements in Eq. (11). Care, then, must be taken in determining what interaction matrix values coincide with the kinematics. The electromagnetic interaction operator is taken as

$$V_{\mathrm{em}}^{(i)\{'\}} = -\frac{e}{m}\frac{1}{2\pi\sqrt{k}}\left(\mathbf{p}_i^{\{'\}}\cdot\boldsymbol{\varepsilon} - \frac{1}{2}\mu_{\mathrm{p}}\boldsymbol{\sigma}_i^{\{'\}}\cdot\mathbf{k}\times\boldsymbol{\varepsilon}\right)$$
$$\text{(in natural units)}\ , \quad (13)$$

where $\boldsymbol{\sigma}$ represents the Pauli spin matrices and $\boldsymbol{\varepsilon}$ is the unit polarization vector of the photon. RSC are to be added as higher orders of m^{-1}. This is discussed later.

Evaluation of the spin space NN t-matrix $\langle S'M', \mathbf{p}'|t^-(E_{\mathbf{p}})|\mathbf{p}, SM\rangle$, $\langle S'M', \mathbf{p}'|t^-(E_{\mathbf{p}})|\mathbf{p}, SM\rangle^*$, involves a choice of specification. Either one expresses them in terms of the spin operators of the two protons via the Wolfenstein parameters [20] or one transforms the electromagnetic spin space matrix elements, $\langle S'M'|V_{\mathrm{em}}^{(i)\{'\}}|SM\rangle$, to the representation in which the relative total spin, S, of the protons is invariant. In studying noncoplanar events, the second is the more convenient method. With the first, the four single scattering spin space NN t-matrix elements will have four distinct scattering planes in general.

A. Center-of-mass frames and gauge invariance

There are a number of reasons for using the CM system to evaluate the T-matrix amplitude; not the least of which are practical ones. First, in the soft photon approximation (SPA) [21], wherein the amplitude is expanded in powers of k, it can be shown that the rescattering term to order k^0 is proportional to the CM momentum itself whence the term may be neglected to leading order. Second, the question of gauge invariance and how well it is satisfied is intimately linked to the choice of reference frame. If the rescattering term is not properly treated, bremsstrahlung calculations are not gauge invariant as, generally, the single scattering terms are not.

However Heller [22] has shown that the $O(k^0)$ terms are gauge invariant for the full amplitude. Nevertheless, for uniqueness and completeness higher orders of k should be included in the rescattering term [14, 15, 23]. There are other gauge terms (due to the momentum dependence of the potential) which have been included in some calculations via minimal methods. They are required to ensure a conserved NN current. In fact the calculations are very sensitive to the gauge and so the choice is important. Currently, by working in the CM frame and using the transverse gauge, we assure gauge invariance with suppression of the rescattering term to leading $O(k^0)$.

The advantage of the CM frame was utilized by Brown in first obtaining the electric quadrupole and magnetic dipole photon angular distributions [14, 24] whereas calculations in the laboratory frame predicted electric dipole distributions only due to the negligence of large rescattering contributions. The inclusion of all terms for the rescattering in Brown's work also assured that gauge invariance was treated properly. This work suggested that the contribution of the rescattering to the photon angular distribution is less than 10%. These calculations were conducted at lower energies and her more recent results [3] at 280 MeV infer that there is a slightly greater effect. This is particularly so at forward proton angles for the cross sections and with the analyzing powers. However, RSC were not included in these studies. Quantitatively they are similar to rescattering effects. Liou and Sobel [6] have shown that they are required for Lorentz covariance.

B. RSC and Lorentz covariance

The form and detail of the RSC included are precisely those given elsewhere [1]. Beginning with the Dirac equation for a proton in an external electromagnetic field, a Foldy-Wouthuysen [25] transformation is performed giving a two-component, positive energy equation for the proton. By comparison with the result from the Hamiltonian of the Pauli-Schrödinger equation, the RSC are obtained. These corrections are additive terms to the nonrelativistic convection and magnetization currents of the electromagnetic operator, although predominantly to the latter. The electric corrections are of $O(m^{-3})$ and the static part of this current, due to its $O(k^{-1})$ behavior, is suppressed with increasing energy. In our calculations we have included terms from the correction due to the summation of the one-particle terms in the Foldy-Wouthuysen reduction [26].

Besides their quantitative importance, the RSC, whether in the CM or the laboratory system, are essential for Lorentz covariance. As demonstrated in Ref. [6], the RSC for bremsstrahlung give quite distinct features in cross sections calculated in either frame, even when the rescattering is included for the laboratory frame calculation. Indeed the RSC are considerably more important in the laboratory system than the rescattering and their omission gives quite unsatisfactory $pp\gamma$ results, particularly at higher energies. However, in the CM system their effects are not nearly as dramatic; being roughly proportional to the CM. The results in both frames converge quite rapidly on including only the first-order RSC. This implies a lack of covariance in the nonrelativistic treatment of the the electromagnetic operator but inclusion of only the $O(m^{-2})$ terms seems to rectify this sufficiently. Nevertheless, quantitatively, the RSC effects are suppressed, as are the rescattering term contributions, provided the CM system is used in calculation. Both effects are then small and comparable.

C. Lorentz transformations to the NN center-of-momentum frame

The NN t matrices are functions of the relative momenta of the two nucleons. For use in $pp\gamma$ calculations it is easiest, then, to work in the CM of the on-shell relative momenta. By use of Lorentz invariants and coordinate rotations, it is straightforward to transform matrix elements to the desired reference frame, whether it be the overall $pp\gamma$ CM frame or the laboratory frame. As the first and last two terms in Eq. (11) are on-shell for the outgoing and incoming relative momenta, respectively, two such frames are required. Also, the NN t-matrix calculation is nonrelativistic so the CM transformation for the two-body NN t matrix is to be effected with nonrelativistic coordinates. In order to be consistent with the relativistic kinematics the momenta therein must be transformed to the CM frame by a Lorentz transformation. We calculate the kinematics in the laboratory frame and transform between frames in such a consistent way. Furthermore, for the first and second terms in Eq. (11) the on-shell momentum, $(\mathbf{p}_1'-\mathbf{p}_2')/2$, is not necessarily colinear to the chosen z axis (the incident beam direction). This is the case even for coplanar events but for noncoplanar events, in addition, the y components cannot be ignored. Thus, a generalized Lorentz transformation is required for reference frames in arbitrary directions.

By considering parallel and perpendicular components in the direction of an arbitrary relative velocity, $\mathbf{v}$, between two reference frames these transformations can be obtained from the initial (unprimed) to the final (primed) system:

$$\mathbf{q}'c = \mathbf{q}c + \left\{ \frac{(\gamma-1)}{\beta^2}(\mathbf{q}c\cdot\boldsymbol{\beta}) - \gamma E \right\} \boldsymbol{\beta} \tag{14}$$

and

$$E' = \gamma \{ E - \mathbf{q}c\cdot\boldsymbol{\beta} \} \ , \tag{15}$$

where $\boldsymbol{\beta} = \mathbf{v}/c$, $\gamma = (1-\beta^2)^{-1/2}$, and $E = \sqrt{(\mathbf{q}c)^2 + (mc^2)^2}$. Together Eq. (14) and Eq. (15) transform as the energy-momentum four-vector. Taking the unprimed frame as the CM frame for the two protons one can derive the CM parameters:

$$\boldsymbol{\beta} = \frac{\mathbf{q}_1'c + \mathbf{q}_2'c}{E_1' + E_2'} \ , \tag{16}$$

$$\boldsymbol{\kappa}c = \frac{1}{2}(\mathbf{q}_1'c - \mathbf{q}_2'c) - \frac{1}{2}\frac{\gamma}{\gamma+1}(E_1' - E_2')\boldsymbol{\beta} \ , \tag{17}$$

$$E_\kappa = \frac{E_1' + E_2'}{2\gamma} \ . \tag{18}$$

The relative velocity vector, $\boldsymbol{\beta}$, is simply that of the NN CM while Eq. (17) gives the CM, $\boldsymbol{\kappa}$, in terms of the nonrelativistic result and a relativistic correction term. Note that for the two-body NN t matrices the remaining relative momenta are off-of-the-energy-shell so, once the two CM are determined via Eqs. (16) and (17), the other three must be transformed as the momenta of independent particles [i.e., $\mathbf{p}_1$, $\mathbf{p}_2$, and $\mathbf{k}$ for terms 1 and 2 in Eq. (11), and $\mathbf{p}_1'$, $\mathbf{p}_2'$, and $\mathbf{k}$ for terms 3 and 4]. The off-shell momentum vectors may be cast into their relative momentum form before or after the frame transformation due to the linearity of the Lorentz transformation.

D. The NN interactions and the NN t-matrix formalism

In our studies, the extended Reid soft core [10] (ERSC), the Paris [8], and Bonn OBEPQ [9] interactions were used as input to the Lippmann-Schwinger equations. The Paris and OBEPQ interactions were derived from field theory but the ERSC is purely phenomenological. Off-shell differences are not solely attributable to differences on the energy shell, i.e., the phase shifts. This is apparent in the off-shell region for bremsstrahlung and is displayed in terms of half-off-shell extension functions [27] or f ratios [28]. In utilizing these interactions, note should be made of the various approximations in the derivation of their NN t matrices which may also lead to off-shell differences: the Paris t matrices were always obtained from the Lippmann-Schwinger equation but the Bonn group developed the OBEPQ t matrices via the relativistic Blanckenbecker-Sugar equation. For the majority of our $pp\gamma$ studies we have used the Paris interaction since our t matrices are solutions of Lippmann-Schwinger equations.

A fourth, phenomenological, interaction, developed in Melbourne [11], has been used in some calculations. Our purpose in using it is to observe the effects in the $pp\gamma$ results obtained using a potential which is quite distinct from the other three but which nevertheless fits the NN phase shifts rather well to 400 MeV. This model interaction was defined in momentum space, featured Gaussian as well as the more usual Yukawa form factors, and was designed to fit on-shell scattering and bound two-body data. One or more of three scalar functions of momentum were used in each two-nucleon channel for each of the "one pion," "two pion," and "ρ" and "ω" mesonlike exchange contributions. Its f ratios are similar to those of the Paris potential in all channels except the tensor channels. Therein due to a much weaker tensor force, the Melbourne results are strongly suppressed. Observables sensitive to the off-shell information of the tensor channels could distinguish between these interactions.

The NN t-matrix elements are calculated most conveniently by taking the direction of the initial relative momentum as the axis of quantization and the azimuthal angle of the final relative momentum as zero; thus following the derivation of Stapp *et al.* [29]. A rotation of the axes to coincide with those of the overall $pp\gamma$ frame is then required. That rotation is dealt with later. In order to calculate the elements, $\langle S'M',\mathbf{p}'|t^+(E_\mathbf{p})|\mathbf{p},SM\rangle$ and $\langle S'M',\mathbf{p}'|t^-(E_\mathbf{p})|\mathbf{p},SM\rangle^*$, as prescribed, the Cartesian coordinate axes may be defined as

$$\hat{\mathbf{x}} = \hat{\mathbf{y}}\times\hat{\mathbf{z}}\ ,\quad \hat{\mathbf{y}} = \hat{\mathbf{p}}\times\hat{\mathbf{p}}'\ ,\quad \hat{\mathbf{z}} = \hat{\mathbf{p}}\ . \tag{19}$$

When the two-body NN t-matrix operator is transformed to relative and center-of-mass variables a partial wave expansion of the reduced mass NN t-matrix operator in momentum space is made. We obtain

$$\langle\mathbf{q}'|t^\pm(\omega)|\mathbf{q}\rangle = \frac{2}{\pi}\lambda\sum_{\substack{JST\\L'LN}} i^{L-L'}\mathcal{Y}^N_{L'SJ}(\hat{\mathbf{q}}')\, t^{JST\pm}_{L'L}(q',q;\omega)\,(\mathcal{Y}^N_{LSJ})^\dagger(\hat{\mathbf{q}})P_T\ , \tag{20}$$

where $\lambda = \hbar^2/m$, P_T is the total isospin projection operator, ω is the relative energy, and q' and q may both be off of the energy shell. $\mathcal{Y}^N_{LSJ}(\hat{\mathbf{q}})$ are the tensor spherical harmonics given by

$$\mathcal{Y}^N_{LSJ}(\hat{\mathbf{q}}) = \sum_{\mu\nu} C^{JN}_{L\mu S\nu}Y_{L\mu}(\hat{\mathbf{q}})|S\nu\rangle\ , \tag{21}$$

where $C^{JN}_{L\mu S\nu}$ are the Clebsch-Gordan coefficients [30, 31], $C^{JN}_{L\mu S\nu} = \langle LS\mu\nu|JN\rangle$, and $Y_{L\mu}(\hat{\mathbf{q}})$ are the spherical harmonics [30, 31]. This NN t matrix relates to the nonrelativistic scattering amplitude [29], $f(\mathbf{q}',\mathbf{q})$, via

$$f(\mathbf{q}',\mathbf{q}) = -\frac{2\pi^2}{\lambda}\langle\mathbf{q}'|t(\omega)|\mathbf{q}\rangle\ . \tag{22}$$

Expanding Eq. (20) between the spin states $|S'\nu',\mathbf{q}'\rangle$ and $|S\nu,\mathbf{q}\rangle$ gives

$$\langle S'\nu',\mathbf{q}'|t^\pm(\omega)|\mathbf{q},S\nu\rangle = \frac{2}{\pi}\lambda\sum_{\substack{JTN\\L'L}} i^{L-L'}C^{JN}_{L'\mu'S\nu'}Y_{L'\mu'}(\hat{\mathbf{q}}')t^{JST\pm}_{L'L}(q',q;\omega)C^{JN}_{L\mu S\nu}Y_{L\mu}{}^*(\hat{\mathbf{q}})P_T\ . \tag{23}$$

Due to parity conservation and the antisymmetry of the wave function [32] there are no singlet-triplet transitions for the two nucleons and so $S' = S$ in this expression. Also, the axes are chosen such that the azimuthal angles are zero for the spherical harmonics, $Y_{L'\mu'}(\hat{\mathbf{q}}')$ and $Y_{L\mu}{}^*(\hat{\mathbf{q}})$, and quantization along the z axis sets the orbital angular momentum projection to zero for the initial beam, i.e., $\mu = 0$. The antisymmetrization of the two proton states limits consideration to $T = 1$ isospin states and results in a multiplicative factor of 2 in the amplitude. Incorporating all of the above leads to the simplified expression

$$\langle S\nu', \mathbf{q}'|t^{\pm}(\omega)|\mathbf{q}, S\nu\rangle = \frac{4\lambda}{\pi} \sum_{\substack{JLL' \\ (S+L+1 \text{ odd})}} i^{L-L'} \sqrt{\frac{2L+1}{4\pi}}\; t^{JST=1\,\pm}_{L'L}(q', q; \omega) C^{J\nu}_{L'(\nu-\nu')S\nu'} C^{J\nu}_{L0S\nu} Y_{L'(\nu-\nu')}(\hat{\mathbf{q}}') , \tag{24}$$

where $\hat{\mathbf{q}}'$ lies in the x-z plane.

Thus the partial wave NN t-matrix elements, $t^{JST=1\,\pm}_{L'L}(q', q; E_q)$, in Eq. (24) must be calculated. The CM NN t matrix must satisfy the Lippmann-Schwinger equation,

$$\langle \mathbf{q}'|t^{\pm}(\omega)|\mathbf{q}\rangle = \langle \mathbf{q}'|V|\mathbf{q}\rangle + \lim_{\eta\to 0} \int d\mathbf{p}' \frac{\langle \mathbf{q}'|V|\mathbf{p}\rangle\langle \mathbf{p}|t^{\pm}(\omega)|\mathbf{q}\rangle}{\omega - \lambda p^2 \pm i\eta} . \tag{25}$$

Taking the partial wave expansion for $\langle \mathbf{q}'|t(\omega)|\mathbf{q}\rangle$, Eq. (20), and the corresponding expression for the NN interaction,

$$\langle \mathbf{q}'|V|\mathbf{q}\rangle = \frac{2}{\pi}\lambda \sum_{\substack{JST \\ L'LN}} i^{L-L'} \mathcal{Y}^N_{L'SJ}(\hat{\mathbf{q}}')\; V^{JST}_{L'L}(q', q)\; (\mathcal{Y}^N_{LSJ})^{\dagger}(\hat{\mathbf{q}}) P_T , \tag{26}$$

yields

$$t^{JST\pm}_{L'L}(q', q; \omega) = V^{JST}_{L'L}(q', q) + \frac{2}{\pi} \sum_{l} \lim_{\eta\to 0} \int_0^{\infty} dp\, p^2 \frac{V^{JST}_{L'l}(q', p) t^{JST\pm}_{lL}(p, q; \omega)}{q_0^2 - p^2 \pm i\eta} . \tag{27}$$

A matrix inversion method [28] was used to solve the partial wave NN t-matrix equations. However, we did not solve for the complex t matrices. Rather, the procedure as per Haftel and Tabakin [33] was used, giving purely real R matrices, $R^{JST}_{L'L}(q', q; \omega)$. They are defined with standing wave boundary conditions and obey an equation analogous to Eq. (27) save that the principle value of the integrals is taken. Those integrals are replaced by grids of Gauss-Laguerre integration points, suitable pole terms subtracted, and matrix inversion performed to obtain $R^{JST}_{L'L}(q', q; \omega)$. A lower and upper form [34] (LU decomposition) of the coefficient matrix is used for this inversion. The fully off-shell t-matrix elements with outgoing boundary conditions, $t^{JST+}_{L'L}(q', q; \omega)$, may then be obtained directly from the R-matrix elements via the Heitler equation. We require only the half-off-shell elements ($q = q_0$; $\omega = \lambda q_0^2$), which relate to the R-matrix solutions explicitly as

$$t^{JST+}_{\mathcal{L}\mathcal{L}}(q', q_0; \omega) = \left\{R^{JST}_{\mathcal{L}\mathcal{L}}(q', q_0; \omega) \left[1 + iq_0 R^{JST}_{\mathcal{L}'\mathcal{L}'}(q_0, q_0; \omega)\right] - iq_0 R_{\mathcal{L}\mathcal{L}'}(q', q_0; \omega) R^{JST}_{\mathcal{L}'\mathcal{L}}(q_0, q_0; \omega)\right\} / \mathcal{D} , \tag{28}$$

$$t^{JST+}_{\mathcal{L}\mathcal{L}'}(q', q_0; \omega) = \left\{R^{JST}_{\mathcal{L}\mathcal{L}'}(q', q_0; \omega) \left[1 + iq_0 R^{JST}_{\mathcal{L}\mathcal{L}}(q_0, q_0; \omega)\right] - iq_0 R_{\mathcal{L}\mathcal{L}}(q', q_0; \omega) R^{JST}_{\mathcal{L}\mathcal{L}'}(q_0, q_0; \omega)\right\} / \mathcal{D} , \tag{29}$$

$$t^{JST+}_{\mathcal{L}'\mathcal{L}}(q', q_0; \omega) = \left\{R^{JST}_{\mathcal{L}'\mathcal{L}}(q', q_0; \omega) \left[1 + iq_0 R^{JST}_{\mathcal{L}'\mathcal{L}'}(q_0, q_0; \omega)\right] - iq_0 R_{\mathcal{L}'\mathcal{L}'}(q', q_0; \omega) R^{JST}_{\mathcal{L}'\mathcal{L}}(q_0, q_0; \omega)\right\} / \mathcal{D} , \tag{30}$$

$$t^{JST+}_{\mathcal{L}'\mathcal{L}'}(q', q_0; \omega) = \left\{R^{JST}_{\mathcal{L}'\mathcal{L}'}(q', q_0; \omega) \left[1 + iq_0 R^{JST}_{\mathcal{L}\mathcal{L}}(q_0, q_0; \omega)\right] - iq_0 R_{\mathcal{L}'\mathcal{L}}(q', q_0; \omega) R^{JST}_{\mathcal{L}\mathcal{L}'}(q_0, q_0; \omega)\right\} / \mathcal{D} , \tag{31}$$

where ($J \geq 0$) $\mathcal{L} = \mathcal{L}' = J$ for uncoupled and ($\mathcal{L} = |J - 1|$, $\mathcal{L}' = J + 1$) for coupled channels. The denominator factor, $\mathcal{D}$, is

$$\mathcal{D} = \left[1 + iq_0 R^{JST}_{\mathcal{L}\mathcal{L}}(q_0, q_0; \omega)\right] \left[1 + iq_0 R^{JST}_{\mathcal{L}'\mathcal{L}'}(q_0, q_0; \omega)\right] + q_0^2 R^{JST}_{\mathcal{L}\mathcal{L}'}(q_0, q_0; \omega) R^{JST}_{\mathcal{L}'\mathcal{L}}(q_0, q_0; \omega)$$

and is on the energy shell. Such matrix inversions require, typically, 32 Gauss-Laguerre points to achieve an accuracy well within one part in 10^3. However for the results given herein, 64 Gauss-Laguerre points have been used throughout and all t matrices have been calculated explicitly from matrix inversion for each on-shell momentum required for the $pp\gamma$ calculation. A cubic spline interpolation was used to give the t-matrix elements for the specific off-shell momenta. Finally we note that a method of continued fractions could also be used instead of matrix inversion. Previous calculations using both methods gave identical results [28].

Our method of solution differs for that used for the TRIUMF calculation [1] in which the half-off-shell extension function was calculated specifically. The two calculations are the same in principle; albeit that Workman and Fearing used relativistic energies for their propagators in the Lippmann-Schwinger equation whereas we use the orthodox nonrelativistic form. The similarities in our $pp\gamma$ observables suggest that the effect of this difference is of little consequence due to the size of the relative momentum values involved and the inherent cancellation in the energy denominators.

It should be noted that both of the amplitudes,

$$\langle S'M', \mathbf{p}'|t^{+}(E_{\mathbf{p}})|\mathbf{p}, SM\rangle$$

and

$$\langle S'M', \mathbf{p}'|t^{-}(E_{\mathbf{p}})|\mathbf{p}, SM\rangle^{*},$$

required according to Eq. (11), can now be obtained directly from Eq. (24) in the NN CM. By use of the relation

$$[t_{L'L}^{JST-}(q',q;\omega)]^* = t_{L'L}^{JST+}(q',q;\omega) \tag{32}$$

they can both be calculated in terms of the partial wave t-matrix elements with outgoing boundary conditions. The spherical harmonics are always real for the chosen axes defined by Eq. (19).

IV. OTHER CONTRIBUTIONS AND CONSIDERATIONS

It has been found that for sufficient convergence in $pp\gamma$ calculations the NN t-matrix elements for all partial waves $J \leq 6$ must be included. All calculations we have made do so except those made using the ERSC potential, which is defined only to $J = 5$. In all calculations we note that the odd J channels have little effect for $J > 4$ but the even J values are important to $J = 6$, particularly as they contain the isovector ($T = 1$) tensor channels. For higher partial waves we use the OPE amplitudes of Workman and Fearing [1, 35] (included for $J > 6$) but they make very little contribution not only to the cross sections but also to the analyzing powers. Nevertheless, all such terms for $J < 20$ were included in our calculations, for completeness.

Contributions from meson exchange currents have been ignored as they are not a first-order effect for $pp\gamma$. They are very small; albeit compulsory for a suitable model of $np\gamma$. Nakayama [2] included these effects in the soft photon limit for which the contribution of the two-body current to $pp\gamma$ is zero. Photon emission from such processes requires the exchange of at least two mesons. Estimations of Ueda [36] suggest an effect of less than 2% for the energies we consider.

Also included, we believe for the first time at higher energies, are the proper off-shell Coulomb scattering amplitudes. However, only the analytic off-shell Coulomb amplitude itself has been included in our calculations. The NN t matrices are still defined as expectation values of free particle states. They are not too different from the elements taken between Coulomb states [37]. In collaboration with the Hamburg group we are developing Coulomb distorted NN t matrices as such are particularly relevant for geometries as used in the recent work at the IUCF Cooler Ring [4], i.e., of measurements made at very forward angles, at which the on-shell Coulomb amplitude approximation breaks down. An estimation of the Coulomb effects at very forward angles, where proton separation is smallest and these effects are expected to be greatest, has not been made as yet.

V. TRANSFORMATION TO FINAL LABORATORY FRAME

It now remains to transform all the various Lorentz frames of the T-matrix amplitude to the chosen single reference frame in which all axes coincide. The observables are evaluated in the laboratory frame and in order to obtain the T-matrix amplitude in this frame it is cast into the form of a Lorentz invariant. For each Lorentz frame, if the amplitude is multiplied by the square roots of all initial and final particle energies, the analogous labatory T-matrix amplitude is obtained via

$$\left\{E_{\mathbf{p}_1'}E_{\mathbf{p}_2'}E_{\mathbf{k}}E_{\mathbf{p}_1}E_{\mathbf{p}_2}\right\}_{\rm lab}|T_{\rm lab}|^2 = \left\{E_{\mathbf{p}_1'}E_{\mathbf{p}_2'}E_{\mathbf{k}}E_{\mathbf{p}_1}E_{\mathbf{p}_2}\right\}_{\rm CM}|T_{\rm CM}|^2 \ . \tag{33}$$

As the NN spin t-matrix elements were calculated in the individual NN CM frame and with the initial relative momentum defining the quantization axis, these amplitudes now need to be rotated to the chosen laboratory frame in which the initial beam direction is the quantization axis and with symmetric proton azimuthal angles. The singlet NN spin T-matrix elements are invariant under rotations so only spin-1 rotation matrices are required to rotate the triplet ($S = 1$) amplitudes to the desired frame. With the axes defined in the NN CM by Eqs. (19) the NN amplitude can be rotated directly from

$$\langle 1\ M',\mathbf{p}'|t^+(E_\mathbf{p})|\mathbf{p},1\ M\rangle = \sum_{mm'} D^1_{M'm'}(\alpha,\beta,\gamma)\langle 1\ m',\mathbf{p}'|t^+(E_\mathbf{p})|\mathbf{p},1\ m\rangle_{NN\ \rm CM}\{D^1(\alpha,\beta,\gamma)\}^\dagger_{mM} \tag{34}$$

and

$$\langle 1\ M',\mathbf{p}'|t^-(E_\mathbf{p})|\mathbf{p},1\ M\rangle^* = \sum_{mm'} D^1_{Mm'}(\alpha,\beta,\gamma)\langle 1\ m,\mathbf{p}'|t^-(E_\mathbf{p})|\mathbf{p},1\ m'\rangle^*_{NN\ \rm CM}\{D^1(\alpha,\beta,\gamma)\}^\dagger_{mM'} \ , \tag{35}$$

where α, β, and γ are the Euler angles [38, 39] and $D^1_{M'M}(\alpha,\beta,\gamma)$ are the Wigner rotation matrices [30, 38]. Note that for the conjugated matrix elements the transpose spin NN t matrix is rotated and gives the transpose matrix in the new reference frame.

For coplanar events only the first and second terms in Eq. (11) require rotation. For noncoplanar events, however, all four terms in Eq. (11) must be rotated. For the third and fourth terms in that equation the NN CM axes are colinear to the chosen laboratory coordinate axes so that, in the y convention [38, 39], β takes on only two values, 0° or 180°. The third rotation occurs in the same plane as the first so that only one of these two is necessary. We choose $\gamma = 0$ in which case the direction cosines are given by

$$\begin{aligned} \sin\alpha &= -\hat{\mathbf{x}}'\cdot\hat{\mathbf{y}} = \hat{\mathbf{y}}'\cdot\hat{\mathbf{x}} \ , \\ \cos\alpha &= \hat{\mathbf{x}}'\cdot\hat{\mathbf{x}} = \hat{\mathbf{y}}'\cdot\hat{\mathbf{y}} \ , \end{aligned} \tag{36}$$

for $\beta = 0$, and by

$$\sin\alpha = -\hat{\mathbf{x}}' \cdot \hat{\mathbf{y}} = -\hat{\mathbf{y}}' \cdot \hat{\mathbf{x}} \,, \qquad \cos\alpha = -\hat{\mathbf{x}}' \cdot \hat{\mathbf{x}} = \hat{\mathbf{y}}' \cdot \hat{\mathbf{y}} \,, \tag{37}$$

for $\beta = 180°$, when transforming from the unprimed to the primed frame. It is to be noted that the direction cosines given in Ref. [1] [Eq. (3.3)] and Ref. [5] [Eq. (5.15)] are not appropriate in this case.

VI. PHASE SPACE AND OBSERVABLES

Using natural units hereafter, for the derivation of the $pp\gamma$ cross section we begin with the expression

$$d\sigma = \frac{(2\pi)^4}{\sqrt{(\mathbf{p}_1 \cdot \mathbf{p}_2 - E_{\mathbf{p}_1} E_{\mathbf{p}_2})^2 - m^4}}\, d\rho\, \overline{\sum_{\text{spins}}} \sum_{\lambda} \left| \sqrt{E_{\mathbf{p}_1'} E_{\mathbf{p}_2'} E_{\mathbf{k}} E_{\mathbf{p}_1} E_{\mathbf{p}_2}}\; T \right|^2 , \tag{38}$$

in which the λ index sums over the polarization states of the photon. The first term on the right-hand side of Eq. (38) is the flux, the third term is the transition amplitude term, and the infinitesimal phase space density, $d\rho$, is given by

$$d\rho = \delta(E_{\mathbf{p}_1'} + E_{\mathbf{p}_2'} + E_{\mathbf{k}} - E_{\mathbf{p}_1} - E_{\mathbf{p}_2})\, \delta^{\,3}(\mathbf{p}_1' + \mathbf{p}_2' + \mathbf{k} - \mathbf{p}_1 - \mathbf{p}_2)\; \frac{d^3\mathbf{p}_1' d^3\mathbf{p}_2' d^3\mathbf{k}}{E_{\mathbf{p}_1'} E_{\mathbf{p}_2'} E_{\mathbf{k}}} \,. \tag{39}$$

It should be noted that each cofactor (the flux, phase space, and amplitude) is invariant and each is represented in the laboratory frame. The flux and phase space can be evaluated explicitly in the laboratory frame quite straightforwardly, and a prescription for the latter can be found in the appendix of Ref. [6]. The phase space factor for coplanar events is

$$F_{\text{coplanar}} = p_1'^2 p_2'^2 \cos\bar{\phi}_\gamma / E_{\mathbf{p}_1'} E_{\mathbf{p}_2'} |D| \,, \tag{40}$$

where all quantities are in the laboratory frame and D is the determinant given by Eq. (A23) in Ref. [6]. The noncoplanar phase space factor can be written in terms of this as

$$F_{\text{noncoplanar}} = F_{\text{coplanar}} \left| \frac{d\bar{\theta}_\gamma}{d\psi_\gamma} \right| \,, \tag{41}$$

where $d\bar{\theta}_\gamma / d\psi_\gamma$ can be deduced easily from Eq. (A38) in Ref. [6]. Note that the absolute value is taken for $d\bar{\theta}_\gamma / d\psi_\gamma$ otherwise $F_{\text{noncoplanar}}$ changes sign at large noncoplanarities, i.e., when $\bar{\theta}_\gamma$ begins to decrease as ψ_γ increases.

Explicitly, the differential cross section is the photon angular distribution and takes the form

$$\frac{d^3\sigma}{d\Omega_1' d\Omega_2' d\psi_\gamma} = \frac{1}{4} \frac{(2\pi)^4}{|\mathbf{p}_1|\, m} F_{\text{noncoplanar}} \sum_{\lambda} \sum_{\substack{S'S \\ M'M}} \left| \sum_j \left\{ \sqrt{E_{\mathbf{p}_1'} E_{\mathbf{p}_2'} E_{\mathbf{k}} E_{\mathbf{p}_1} E_{\mathbf{p}_2}}\; \langle S'M' |T| SM \rangle \right\}_j \right|^2 , \tag{42}$$

where the factor of $\frac{1}{4}$ is due to the averaging over initial spin projection quantum numbers and the index j sums over all Lorentz frames. The coplanar result is directly given by Eq. (42) also, as in this case $\psi_\gamma = \bar{\theta}_\gamma$ and $d\bar{\theta}_\gamma / d\psi_\gamma = 1$.

The summation of the amplitudes in Eq. (42) is affected if we cast the operator in the form

$$T = \boldsymbol{\varepsilon} \cdot \mathbf{M} \,, \tag{43}$$

with the vector $\mathbf{M}$ and photon polarization, $\boldsymbol{\varepsilon}$, in the spherical basis. In the transverse gauge one can define an orthonormal set of basis vectors $(\hat{\mathbf{e}}_{-1}, \hat{\mathbf{e}}_0, \hat{\mathbf{e}}_1)$ such that $\mathbf{e}_0 = \mathbf{k}$, and $\hat{\mathbf{e}}_{\pm 1}$ represent the polarization states, ε_λ. The dot product [Eq. (43)] may be evaluated for each Lorentz frame and all states then summed.

For the analyzing power the amplitudes for each state undergo a transformation to the uncoupled two-particle spin basis,

$$|\tfrac{1}{2}\tfrac{1}{2} m_1 m_2\rangle = C^{SM}_{\frac{1}{2}m_1 \frac{1}{2}m_2} |SM\rangle \,, \tag{44}$$

where m_1 and m_2 are the spin projection quantum numbers for each proton. This facilitates matrix multiplication with the Pauli spin matrices quantized along the laboratory beam axis so that the analyzing power is given by

$$A_i = \frac{\mathrm{Tr}\,(\boldsymbol{\sigma}\cdot\hat{\mathbf{n}}_i\,T^\dagger T)}{\mathrm{Tr}\,(T^\dagger T)} = \frac{\sum_{m_1 m_2 m_1' m_2' m_3 m_4}\langle m_1 m_2\,|\sigma_i|\,m_1' m_2'\rangle\langle m_3 m_4\,|T|\,m_1' m_2'\rangle^*\langle m_3 m_4\,|T|\,m_1 m_2\rangle}{\sum_{n_1' n_2' n_1 n_2}\langle n_1' n_2'\,|T|\,n_1 n_2\rangle^*\langle n_1' n_2'\,|T|\,n_1 n_2\rangle}\,, \tag{45}$$

where $\hat{\mathbf{n}}_i$ is a unit vector that lies along one of the Cartesian axes and $\langle m_1 m_2\,|\sigma_i|\,m_1' m_2'\rangle$ are the Pauli spin matrix elements in the uncoupled basis of the two protons. Note that the analyzing power is completely independent of the phase space factor. Finally we note that for coplanar events, by symmetry, $A_x = 0 = A_z$.

VII. RESULTS AND DISCUSSION

In this section we make a comparison between the four interactions used for the coplanar geometry and subsequently present a partial wave analysis for this geometry. In view of the similarity of the observables obtained with all forces, the Paris interaction is used as representative of the "realistic" NN interaction for most of the calculations herein. Most of the results focus on 280 MeV incident energy as a precursor to the off-shell studies made in the most sensitive off-shell region. Our noncoplanar results for the cross section and analyzing power components are then presented and are followed by the results of the off-shell calculations for both coplanar and noncoplanar geometries. For simplicity and because asymmetric geometries do not offer much new information for our current purposes, only noncoplanar events involving symmetric proton emission angles are considered. As has been established, large proton separation angles approach the elastic limit (i.e., as $\bar{\theta}_1 + \bar{\theta}_2 \to 90°$) [5] and for the observables of interest the strongest off-shell behavior occurs at small detector angles. Given that the noncoplanar kinematics show that the photon magnitude actually increases out of the plane it suggests that noncoplanar geometries may produce further off-shell information, particularly for the P waves in the $pp\gamma$ reaction. The $pp\gamma$ reaction is most sensitive to the P waves close to pion threshold and strongly constrains their behavior [18] but has little bearing on the S waves, for which $np\gamma$ may yield more information.

We specify as "on-shell calculations" those in which all the half-off-energy-shell NN t matrices entering the calculation are forced to be on shell. Essentially one uses only the NN elastic scattering amplitudes and thus the magnitudes of the off-shell momenta are set equal to the on-shell momentum magnitudes in all the partial wave NN t-matrix amplitudes. For a given (JST) channel with orbital angular momentum quantum numbers L and L' one has

$$t^{JST}_{L'L}(q', q; E_q) \to t^{JST}_{L'L}(q, q; E_q), \tag{46}$$

where q and q' are the on- and off-shell momentum magnitudes, respectively. This is in contrast to the soft photon approximation [21] in which the $pp\gamma$ amplitude is expanded in the limit where the photon momentum goes to zero ($k \to 0$) and is effectively an on-shell average of the total amplitude. By forcing the NN t matrix elements to be on shell in this way one can eliminate all off-shell information from the single scattering amplitudes.

The electric and magnetic contributions to the cross section are discussed in some detail for a wide range of energies and kinematics. Finally, we look at the importance of incorporating the higher partial waves to the NN t matrices and the effect of including the RSC as compared to experimental data.

A. On- and off-shell behavior of the interactions

In Figs. 2 and 3 the TRIUMF data [16] for the extreme proton angles are compared with our theoretical calculations for four interactions. The Bonn OBEPQ, Paris, and ERSC results are displayed in these figures by the solid, dashed, and dot-dashed curves, respectively. The Melbourne potential is represented by the dotted curve. Using the on-shell approximation, all four interactions lead to very similar results for the two events considered, as could be expected, since all four fit the relevant NN elastic data very well. The $(28.0°, 27.8°)$ $pp\gamma$ data [i.e., LEP proton angle is $\theta = 28.0°$ (see Sec. II)], cannot distinguish between the on- and off-shell calculated results. However, from the $(12.0°, 12.4°)$ results, clearly the on-

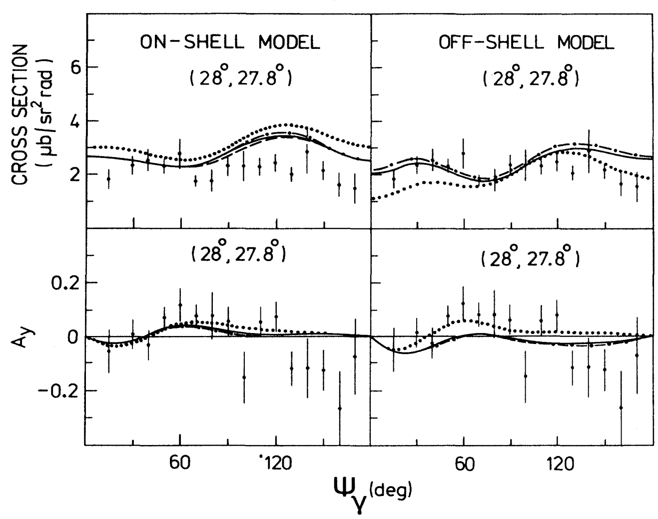

FIG. 2. On-shell model and off-shell model cross section and A_y at 280 MeV for the $(28°, 27.8°)$ coplanar geometry compared with the TRIUMF data for the four interactions used herein: Bonn OBEPQ (solid lines), Paris (dashed lines), ERSC (dot-dashed lines), and Melbourne (dotted lines). Note that for all results we use the convention (LEP, HEP) where the angle on the left (right) represents the low (high) energy proton.

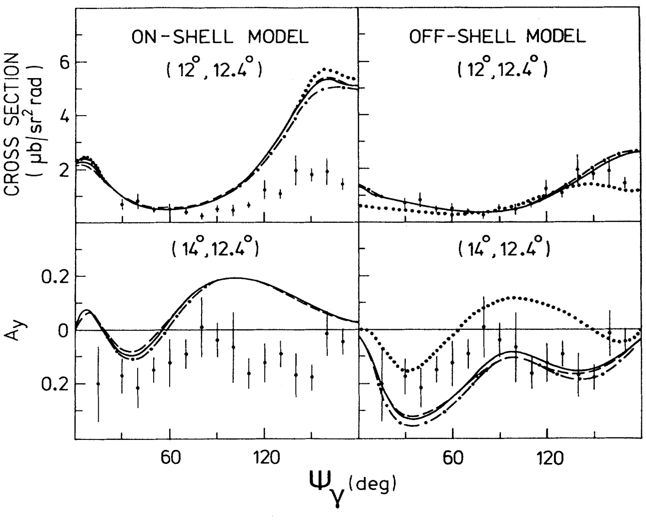

FIG. 3. On-shell model and off-shell model cross section for the $(12°, 12.4°)$ and A_y for the $(14°, 12.4°)$ coplanar geometry at 280 MeV compared with the TRIUMF data for the four interactions as identified in Fig. 2.

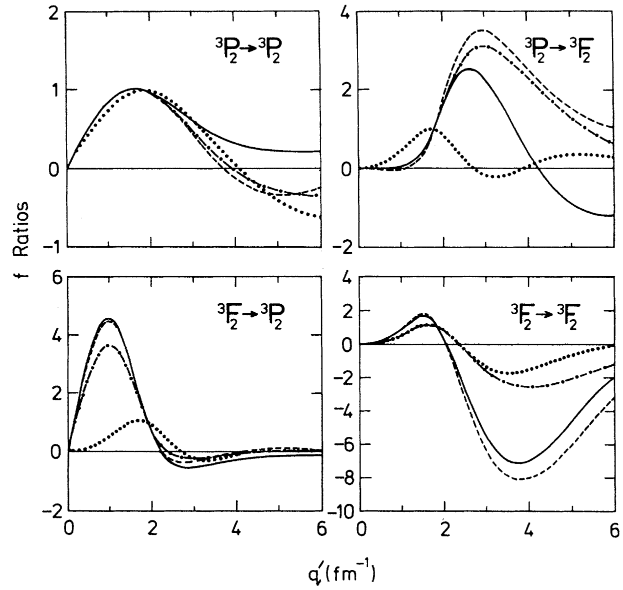

FIG. 4. The f ratios for the $^3P_2$ -$^3F_2$ channels at a laboratory energy of 300 MeV. The curves represent the interactions as in Fig. 2.

shell curves overshoot the data at larger photon angles. Forward proton angles lie in the sensitive off-shell region. Proper off-shell calculations fit the data very reasonably in Figs. 2 and 3 for both observables. These comparisons give measure to the importance of the proper treatment of off-energy-shell properties of the t matrices in $pp\gamma$ calculations. For both observables, cross section and analyzing power, A_y, the similarity of the results obtained using these t matrices show that the current experimental precision does not allow us to distinguish between "realistic" interactions [40]. These results also show that off-shell properties of the t matrices influence predictions of A_y most markedly.

The three conventional interactions, Bonn OBEPQ, Paris, and ERSC, all yield good fits to the low partial wave NN channel phase shifts and all are predicated upon an underlying particle exchange theory to one extent or another. Such is an important constraint. The phenomenological, velocity dependent interaction developed in Melbourne [11] to provide as good a fit to the empirical on-shell data as possible, when used in these $pp\gamma$ calculations, gave comparable on-shell results. However, off of the energy shell it is very different to the other interactions which is attributable to off-shell differences which lie, primarily, in the tensor channels.

As double scattering (rescattering) contributions were not included the off-shell attributes of the NN t matrices can be observed directly. The behavior of the $pp\gamma$ observables are reflected in the half-off-shell f-ratio function of the interactions [28] which stress the off-shell variations of the R matrices, $R^{JST}_{L'L}(q', q_0; \omega)$. As demonstrated in Fig. 4, the Melbourne interaction is the only one that extrapolates differently away from the on-shell point for the off-diagonal NN t-matrix elements. It gives off-shell values particularly different to those of the other three interactions for off-shell momenta of up to 1.5–2.0 fm^{-1} away from the on-shell point which is the typical bremsstrahlung off-shell region for the kinematics we consider. This behavior corresponds almost directly to the differences in A_y between the interactions, as is most evident from the $(14.0°, 12.4°)$ results in Fig. 3. We demonstrate later that the marked decrease in the cross section calculated values is evidence of the weaker tensor coupling of the Melbourne interaction, a result in contradiction with the suggestion of Brown *et al.* [3] that a weaker tensor force may result in a larger cross section.

B. Partial wave study for coplanar geometries

Coplanar geometry $pp\gamma$ cross sections and analyzing powers are shown in Figs. 5 and 6 for 280 MeV incident energy and symmetric proton angles, $\theta_1 = \theta_2 = \theta = 12°$ and 30°, respectively. The complete results, with t matrices taken off of the energy shell, for the Paris interaction are given by the continuous lines in each case. In the top section of these figures the complete results are compared with the on-shell approximation (for all channels) results, the latter displayed by the dashed curves. For both proton polar angle choices, in the middle and bottom sections of this diagram results are given when calculations are restricted to include but a finite set of two-nucleon channels.

Adding successive partial waves for the observables may give further insight as to the channel admixtures, interference, and off-shell behavior. In the middle section of Fig. 5 the contributions to the cross sections due solely to the $^1S_0$ channel are displayed by the long-dashed curve. It is not very significant. When the $^3P_0$ channel is included, whence all $J = 0$ contributions are used in the calculation, the results are as depicted by the short-

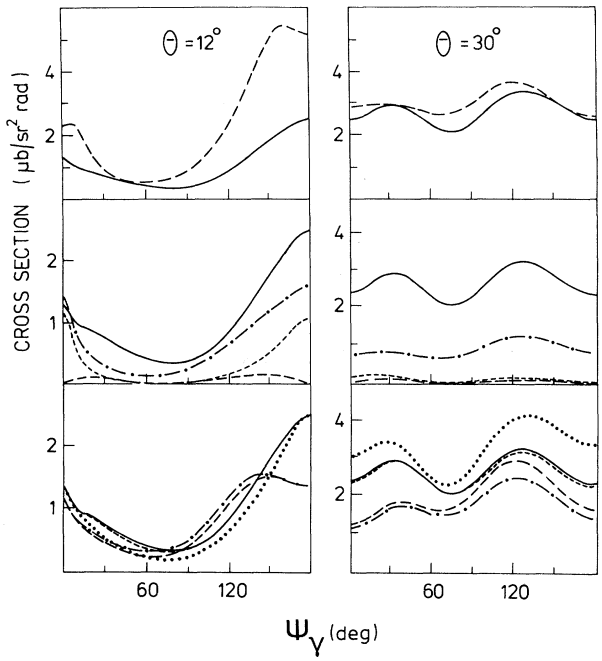

FIG. 5. Coplanar cross sections at 280 MeV for $\theta_1 = \theta_2 = \theta = 12°$ (left panels) and $\theta = 30°$ (right panels) using the Paris interaction. The off-shell model calculation is designated by the solid curve in all cases. The top panels show the on-shell model calculation by the dashed lines. The middle panels show the calculations including only ${}^1S_0$ (long-dashed), (${}^1S_0 + {}^3P_0$) (short-dashed), and (${}^1S_0 + {}^3P_0 + {}^3P_1$) (dot-dashed) partial waves. The bottom panels show the calculation including all ($T = 1$) $J \leq 2$ (dotted) and all ($T = 1$) $J \leq 4$ channels (short dashed). These same two cases excluding the off-diagonal NN t-matrix elements are shown by the long-dashed and dot-dashed lines, respectively.

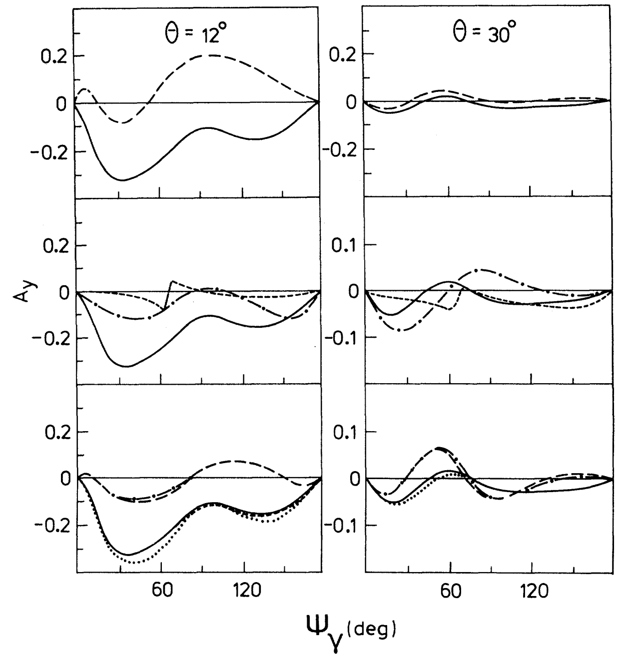

FIG. 6. Coplanar A_y at 280 MeV for $\theta_1 = \theta_2 = \theta = 12°$ (left panels) and $\theta = 30°$ (right panels) using the Paris interaction. The curves are as designated in Fig. 5.

dashed curves. The $J = 0$ contributions are evidence of a predominantly electric character for both $(12°, 12°)$ and $(30°, 30°)$ cases. The dot-dashed curves then portray the inclusion of all $J = 0$ and $J = 1$ channels. Thereby about one-half of the complete cross section is obtained. Adding further channels into the cross section summations give the results shown in the bottom panels of Fig. 5. These include the tensor coupled channels. The importance of the coupling has been shown by Brown [14] for the cross section at lower energies. It is stressed further herein as the results of adding all channels with $J \leq 2$ and with $J \leq 4$ are shown by the dot and the small-dashed curves, respectively. If the coupling is ignored then the results are those displayed by the dashed and dot-dashed curves, respectively. There is an obvious difference to the proper coupling results.

Comparison of the full calculation results for θ of 12° and 30° as one adds successive J channels shows considerable variation as well. As mentioned, for $\theta = 12°$, the P waves give the dominant contributions to the cross section. By and large, however, successive component (J) amplitudes constructively interfere for the $\theta = 12°$ case to give the complete cross section. The off-diagonal NN t-matrix elements are responsible for the enhanced peak at the backangles. However, there is significant destructive interference due to these off-diagonal elements in the middle photon angles, and the off-diagonal components give most significant effects at large proton scattering angles. The $\theta = 30°$ results, on the other hand, are not very sensitive to the proper off-shell character of the t matrices and are not so strongly determined by the ${}^3P_0$ and ${}^3P_1$ channels. This cross section is dominated by the $J = 2$ tensor coupled states albeit that the higher J-channel contributions have destructive interference properties. The on-diagonal and off-diagonal tensor elements are equally important. Also, in contrast to the $\theta = 12°$ cross section, only constructive interference is observed from the off-diagonal elements for all photon angles.

The same results but for the analyzing power, A_y, are displayed in Fig. 6. As for the cross sections, A_y reflects how the forward proton angles are the sensitive off-shell region for the Gottschalk geometry [13] and the on-shell approximation is particularly poor. Effectively, though, the on-shell approximation results and the full calculations are indistinguishable for $\theta = 30°$. For $(30°, 30°)$ it can be seen how the off-diagonal terms largely determine the final structure of A_y, as would be expected from the analysis of the cross section. However, this is also the case, and more dramatically so, for $(12°, 12°)$ in which these elements almost solely dominate the final shape of A_y. The fact that these terms are not the main contributors to the $(12°, 12°)$ cross section demonstrates the specific sensitivity of A_y to the off-diagonal t-matrix elements. Furthermore, the weaker off-diagonal tensor contributions of the Melbourne interaction are evident from a comparison of Figs. 5 and 6 with Figs. 2 and 3. For these observables the calculation for the Melbourne interaction lies closer to the curves excluding the off-diagonal terms for the other interactions.

C. Results of noncoplanar observables

For bremsstrahlung initiated by 280 MeV incident energy protons with proton polar angles of 12°, there is a kinematic limit to the symmetric azimuthal angle, $\bar{\phi}$, of $\bar{\phi}_{\max} = 9.6°$. This provides a reasonable angular range for studying $pp\gamma$ as a function of $\bar{\phi}$. In Fig. 7 we show the variation with $\bar{\phi}$ of the complete results for the cross sections and for all three analyzing power components displayed as functions of the polar angle ψ_γ (see Sec. II A). The azimuthal angle is shown in steps of 2° and it is evident, by scanning left to right in Fig. 7, that each variable displays a distinctive variation. The cross sections vary most noticeably at the backscattered photon angles, increasing to a maximum near 4° out of the reference x-z plane. Thereafter, the characteristic falloff begins due to the decrease in the total T-matrix amplitude [5], approaching the kinematic limit. The phase space factor plays a major role in the structure of the cross section. At 280 MeV, for coplanar events, it is quite constant for the larger proton angles, $\bar{\theta}$, but is decidedly smaller for perpendicular photon emissions ($\bar{\theta}_\gamma \sim 90°$) at forward proton angles. Equivalently, for noncoplanar scattering, the phase space factor decreases for perpendicular photon emission, but this behavior is more pronounced for larger $\bar{\theta}$ values.

The analyzing power, A_x, is identically zero in the coplanar geometry (as is A_z) but by $\bar{\phi} = 6°$ it is some 15% at around $\psi_\gamma = 60°$. It retains its structure until the noncoplanar limit is approached. The swift change in sign for A_x near the noncoplanar limit occurs at about $\bar{\phi} = 8°$: the point at which the backscattered photons become forward scattered, as they approach the "limiting photon". Only the x component of the analyzing power is finite at the kinematic limit for $\bar{\theta}_1 = \bar{\theta}_2$, where the "limiting photon" momentum lies in the y-z plane with $\bar{\phi}_0 < 90°$.

The y component, A_y, of the analyzing power attains its greatest magnitude for coplanar events, as events there are perpendicular to the chosen y axis. Out of the plane, A_y shows a steady decrease to zero without any structural changes. Unlike A_x, A_y does not change radically as a function of $\bar{\phi}$. In comparison, the A_z component varies quite rapidly from $\bar{\phi} = 0$ to its peak magnitude (for $\psi_\gamma \simeq 120°$) near $\bar{\phi} = 4°$. Beyond this it remains steady to $\bar{\phi} = 6°$ and subsequently decreases to

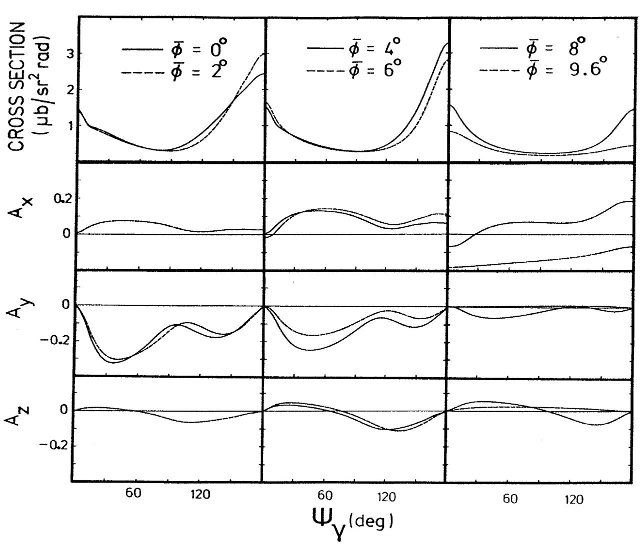

FIG. 7. Cross sections and analyzing powers at 280 MeV for $\bar{\theta}_1 = \bar{\theta}_2 = \bar{\theta} = 12°$ and symmetric proton azimuthal angles, $\bar{\phi}$, as labeled. The results are for the Paris interaction.

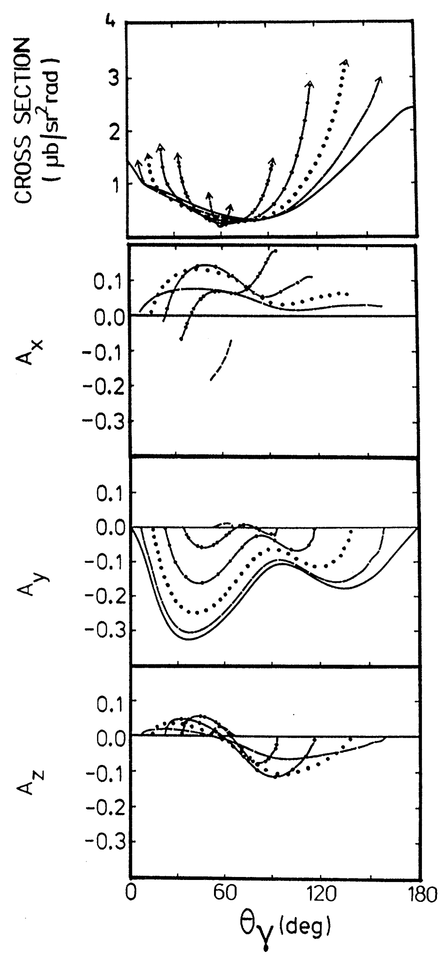

FIG. 8. Cross sections and analyzing powers at 280 MeV using spherical polar coordinates. The calculations are equivalent to those in Fig. 7 and the curves represent the symmetric spherical polar proton angles $\theta_1 = \theta_2 = \theta = 0$ (solid lines), $\theta = 12.16°$ (long-dashed lines), $\theta = 12.64°$ (dotted lines), $\theta = 13.40°$ (dot-dashed lines), $\theta = 14.39°$ (double-dot-dashed lines), $\theta = 15.32°$ (dashed lines).

zero, much like A_y.

We have calculated, also, the analogous observables to those shown Fig. 7 in the spherical polar geometry as a function of the photon spherical polar angle, θ_γ. These results are shown in Fig. 8. A coordinate transformation was made and the curves in Fig. 8 represent the same $pp\gamma$ calculations as for Fig. 7. The transformations were made via [6]

$$\begin{aligned}
\tan\phi_1 &= \frac{\tan\bar{\phi}_1}{\sin\bar{\theta}_1}, \quad \tan^2\theta_1 = \tan^2\bar{\theta}_1 + \left(\frac{\tan\bar{\phi}_1}{\cos\bar{\theta}_1}\right)^2, \\
\tan(\pi-\phi_2) &= \frac{\tan\bar{\phi}_2}{\sin\bar{\theta}_2}, \quad \tan^2\theta_2 = \tan^2\bar{\theta}_2 + \left(\frac{\tan\bar{\phi}_2}{\cos\bar{\theta}_2}\right)^2, \\
\tan(2\pi-\phi_\gamma) &= \frac{\tan\bar{\phi}_\gamma}{\sin\bar{\theta}_\gamma}, \quad \tan^2\theta_\gamma = \tan^2\bar{\theta}_\gamma + \left(\frac{\tan\bar{\phi}_\gamma}{\cos\bar{\theta}_\gamma}\right)^2.
\end{aligned} \tag{47}$$

The restricted photon polar angle (θ_γ) emissions as a function of increasing proton spherical polar angles $\phi = \phi_1 = \phi_2$ and $\theta = \theta_1 = \theta_2$ are evident. The cross section diverges as it asymptotes towards the minimum and maximum emission angles of θ_γ for the noncoplanar events. These same restricted θ_γ values appear for the analyzing power components at the same noncoplanarity. However these observables are convergent at the end points as the divergence in the cross section is due to the phase space factor. The general features of the observables are otherwise similar to those in the Harvard noncoplanar geometry. Had the calculations been made precisely at the noncoplanar limit with spherical polar coordinates, $\bar{\phi} = \bar{\phi}_{\max}$, the cross section would not exist and the analyzing power component values would be at one point corresponding to the "limiting photon."

The integrated (over ψ_γ) cross sections are displayed for proton angles of 12° and 30° at 280 MeV in Fig. 9. The complete results are shown by the continuous curves while the electric and magnetic components are shown separately by the long- and short-dashed curves, respectively. Note the different noncoplanar limit in each case. For $(30°, 30°)$ the falloff near the noncoplanar limit is almost linear while for $(12°, 12°)$ the integrated cross section is virtually constant to $\bar{\phi} = 4°$ and begins to drop slightly more rapidly. This is a feature which is characteristic of forward proton angle scattering. In the TRIUMF experiment [16] acceptance of noncoplanar events did not involve major variations for the coplanar measurements [41]. Our results support this fact but the decrease in the cross section out of the plane, nevertheless, may have to be considered before specifying any coplanar cross section variation. It should be noted, also, that the cross section falloff is similar at pion threshold as it is for lower energies as the reduction in the total T-matrix amplitude is not particularly sensitive to energy.

The slower decrease in the $(12°, 12°)$ noncoplanar cross section is due to the convection current and its interference with the magnetization current component. At forward proton angles this interference seems to be unaffected with increasing noncoplanar angle, $\bar{\phi}$. The destructive coplanar interference increases with increasing noncoplanarity for $\bar{\theta} = 30°$. In fact, it is the interference that causes the falloff to be so dramatic for larger proton angles. Further consideration of electric and magnetic component effects is given later.

In probing $pp\gamma$ for off-shell NN t-matrix effects it would seem that the azimuthal angle, $\bar{\phi} = 4°$, is the most desirable noncoplanarity to choose as this is the region in which all of the observables, except A_y, reach their peak magnitudes and the integrated cross section begins to diminish.

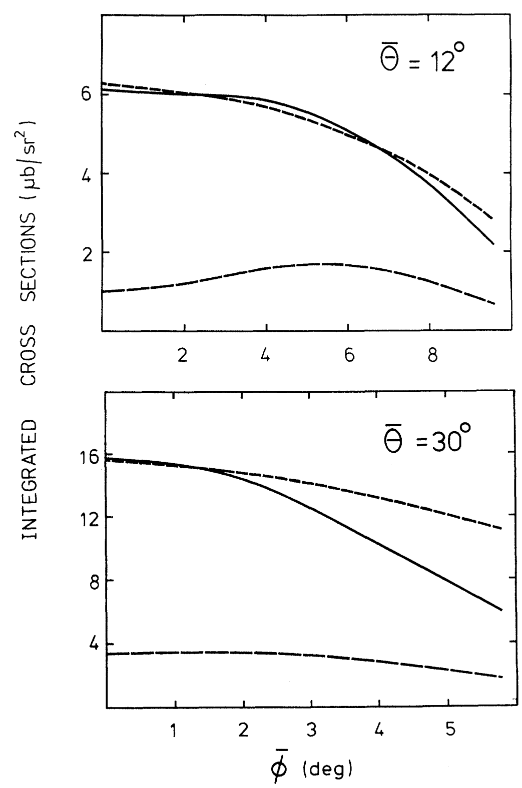

FIG. 9. Integrated cross sections at 280 MeV for the Paris potential as a function of $\bar{\phi}$ for the $\bar{\theta} = 12°$ (top) and $\bar{\theta} = 30°$ (bottom) geometries. The full calculation is the solid line. The electric and magnetic contributions are represented by the long-dashed and short-dashed lines, respectively. Note that these have been integrated for ψ_γ values of 0° to 360°.

D. Off-shell behavior for general kinematics

In Fig. 10 calculated cross sections and analyzing powers, A_y, are displayed for two cases in which the incident energy is 280 MeV with symmetric proton opening angles of $\bar{\theta} = 12°$. On the left are given the coplanar ($\bar{\phi} = 0$) results while on the right the azimuthal angle, $\bar{\phi}$, was set at 4°. The continuous lines in all of these graphs depict the $pp\gamma$ results found using the full off-the-energy-shell Paris t matrices. In the top section the complete cross sections are compared with the on-shell approximation (dashed lines). The A_y observables given by those calculations are compared in the third section of the figure. As has been noted previously [18, 40], the full off-shell properties of the Paris interaction markedly reduce the small and large photon emission angle cross section as compared to the on-shell approximation. This off-shell dependence is slightly enhanced 4° out of the plane at the extreme forward and backward photon angles. The A_y values are affected even more dramatically although the differences between full and on-shell approximation results lessen as the kinematics become more noncoplanar.

The other diagrams in Fig. 10 give the cross sections and A_y when the complete calculations are varied by having only one individual partial wave channel taken as on shell. The long-dashed curves were obtained by taking the $^1S_0$ channel on shell and the short-dashed, dotted, and dot-dashed curves were obtained by taking the $^3P_2$ -$^3F_2$, $^3P_0$, and $^3P_1$ channels individually on shell, respectively. In the coplanar cross sections the greatest variation from the full calculation occurs if $^3P_0$ or $^3P_1$ is put on shell. Hence, it can be seen how the fully off-shell properties of those channels are most important in determining the forward proton scattering cross sections. As the reaction becomes noncoplanar the off-shell properties of the $^1S_0$ channel increasingly influence results before the characteristic fall in the cross section comes into play close to the noncoplanar limit. This is related to the increase in the electric contribution with noncoplanarity for the integrated cross section. The $^1S_0$ channel, on the other hand, has little influence on A_y, even for noncoplanar events. Our results show the marked influence of the $^3P_2$ -$^3F_2$ channels off of the energy shell and we note the off-shell properties of $^3P_1$, so important in specifying the cross section, have a much lesser effect in the analyzing power calculations.

As one goes to noncoplanar geometries, A_x and A_z rapidly become comparable to A_y. This presents an opportunity to obtain further information about off-shell NN t matrices from studies of these observables. The results of our calculations for the three components of the analyzing power at 280 MeV, (12°, 12°), and azimuthal

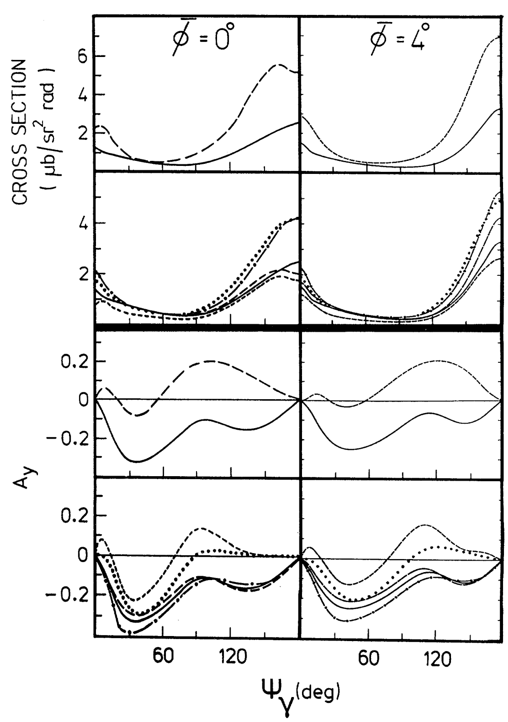

FIG. 10. Calculated cross sections and A_y at 280 MeV for $\bar{\theta} = 12°$ in the coplanar (left) and $\bar{\phi} = 4°$ (right) geometries using the Paris interaction. The solid curve is the full calculation in all cases. In the upper panels for each observable the dashed curves represent the on-shell model calculation. The lower panels for each observable display the results of keeping only one individual partial wave channel on the energy shell. The channels $^1S_0$ (long-dashed), $^3P_2$ -$^3F_2$ (short-dashed), $^3P_0$ (dotted), $^3P_1$ (dot-dashed) are kept individually on shell.

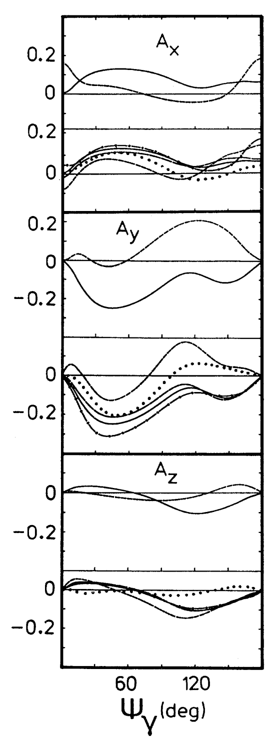

FIG. 11. The analyzing power components at 280 MeV for the $\bar{\theta} = 12°$ and $\bar{\phi} = 4°$ geometry using the Paris potential. The curves for each observable are designated as in Fig. 10.

angle, $\bar{\phi} = 4°$, are displayed in Fig. 11. The complete result is shown by the continuous curves in each segment. The on-shell model results are shown by the large-dashed curves in the top part of each section in the diagram. The on-shell calculation has quite a different variation in comparison to the off-shell result for the three components. A_y still shows distinguishable off-shell character, as it does in the coplanar case, although this may not be so for the other components, given current experimental error.

Partial wave analyses of these analyzing power components are given in the bottom part of each section and indicate, again, the important role of the tensor coupled channels in defining results. Recall that these graphs represent the complete result with a single channel taken in the on-shell approximation. Four such calculations are compared with the complete one. They are displayed by the long-dashed, short-dashed, dotted, and dash-dotted lines for the $^1S_0$, $^3P_2$ -$^3F_2$, $^3P_0$, and $^3P_1$ channel cases, respectively.

The $^3P_2$ -$^3F_2$ and $^3P_0$ channels share the major off-shell contributions for A_x. When the $^3P_2$ -$^3F_2$ channels are kept on shell A_x takes on more of the on-shell structure. The partial wave contributions for A_y are very similar to the equivalent coplanar geometry ($\bar{\phi} = 0$), showing its greatest sensitivity to the $^3P_2$ -$^3F_2$ channels and to $^3P_0$ at photon backangles. It is the off-shell properties of this, the $^3P_0$ channel, to which the A_z component is most sensitive. Although the on-shell $^3P_2$ -$^3F_2$ coupled channels have a slight influence on the off-shell curves, as shown in the bottom section of Fig. 11, keeping the $^3P_0$ channel on shell gives virtually the fully on-shell result.

As a final check of the role of these channels, calculations were made using our phenomenological Melbourne potential. With this force the off-shell results for A_x and A_y differed significantly from those shown in Fig. 11, as do the results in Figs. 2 and 3. The full analyzing power results are very similar to the on-shell model calculation, due largely to the much weaker tensor force of this interaction. However, for A_z, given the dominance of the $^3P_0$ channel, the calculation for all four interactions are almost identical.

Thus, the off-shell dependence of A_y in the coplanar geometry, particularly due to the effects of the tensor channels, is observed also with noncoplanar geometry. The structure of the three analyzing power components show diverse dependencies on the exact off-shell properties of the $T = 1$ NN t-matrix channels. In particular, their off-shell dependence is almost completely dominated by the $^3P_2$ -$^3F_2$ and $^3P_0$ channels, for which each component is more sensitive to either one or the other.

E. Electric and magnetic contributions to the $pp\gamma$ cross section

Bremsstrahlung amplitudes involve the static electromagnetic interaction, Eq. (13), so that all calculated results can be divided into electric $(\mathbf{p}_i^{\{'\}} \cdot \boldsymbol{\varepsilon})$ and magnetic $(\boldsymbol{\sigma}_i^{\{'\}} \cdot \mathbf{k}\times\boldsymbol{\varepsilon})$ components. The separation of these components has been made previously by Brown and explicit results of their behavior are also displayed in a recent publication [3]. The electric or convection current amplitudes lead to cross sections that vary as $1/k$ while the magnetization current gives rise to a variation with k. Electric contributions, therefore, diminish in importance with the energy of the emergent photon and thence also with the selected kinematics. Symmetric coplanar geometries, $(12°, 12°)$ and $(30°, 30°)$, were used with proton incident energies of 50, 150, and 280 MeV to calculate the separate electric and magnetic contributions to the $pp\gamma$ cross sections. Those results are displayed in Fig. 12; the 50 MeV values in the top section and the 280 MeV results at the bottom. In each case the complete result, including RSC, is given by the continuous curve while the electric and magnetic cross sections are portrayed by the long-dashed and short-dashed curves, repectively. We note first that the electric component gives cross sections of quadrupole form, in contrast to the smooth, relatively featureless, magnetic cross sections. Despite the $1/k$ behavior, for the $\bar{\theta} = 30°$ case, the electric part, nevertheless, slightly rises with energy. However, for $\bar{\theta} = 12°$, the larger k^{-1} factor, due to the forward emission of protons, overwhelms other contributions to actually drop the electric cross section. The magnetic part rises almost isotropically for $\bar{\theta} = 30°$, and rather rapidly, whereas at forward proton angles it is not isotropic and increases quite slowly. Due to this behavior, at higher energies the larger proton angle cross sections retain their quadrupole shape reflecting the structure of the convection current amplitudes but with magnitudes determined largely by the magnetization current amplitudes. For forward proton scattering the magnetization

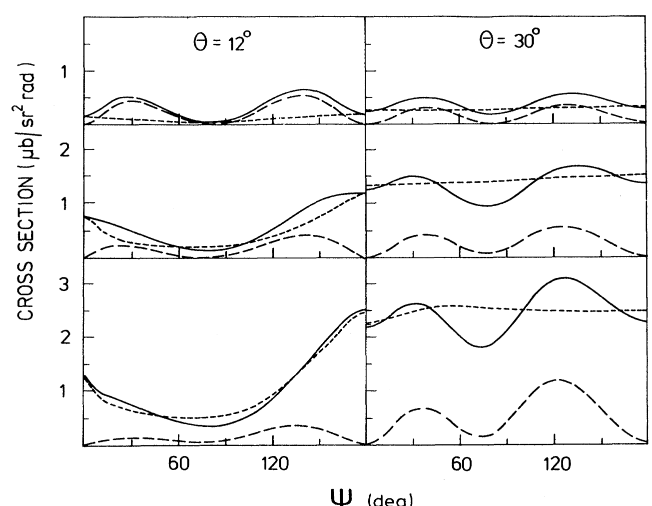

FIG. 12. Calculated coplanar cross sections for the $\theta = 12°$ (left panels) and $\theta = 30°$ (right panels) geometries using the Paris potential. These are displayed for incident energies of 50 MeV (top panels), 150 MeV (middle panels), and 280 MeV (bottom panels). The solid curve represents the full result. The long-dashed and short-dashed lines are for the electric and magnetic contributions, respectively.

current contribution almost completely dominates, as do the NN triplet P waves thereto. The electric and magnetic interference is a major effect for $pp\gamma$ at all coplanar proton emission angles and energies to pion threshold. The enhanced destructive interference is responsible for the reduction of the cross section about the minimum at higher energies.

Suppression of the electric component with increasing energy is one reason for the minor role played by the $^1S_0$ channel in the Gottschalk geometry [13] since the magnetic effects from singlet states are also very strongly suppressed. This role is further reduced by the fact that the major scattering process for $NN\gamma$ is the one in which photon emission precedes the strong interaction event [42]. For $pp\gamma$ these terms are largely cancelled in the full T-matrix amplitude. This can be seen most easily in the CM frame by considering Eq. (13) and the electromagnetic spin matrix elements, $\langle S'M'|V_{\rm em}^{(i)\{'\}}|SM\rangle$, in the first and second terms of Eq. (11). Although at 50 MeV the electric term is still significant (whence the $^1S_0$ channel will influence measurements there) its suppression at higher energies means that $pp\gamma$ affords us an opportunity to study the properties of other two-nucleon channel t matrices and, in particular, those of the coupled amplitudes for the $T = 1$ set. We note that this is not the case with $np\gamma$ which involves other quite different ($T = 0$) two-nucleon channel contributions. For $np\gamma$ the two-body current (also largely suppressed for $pp\gamma$) is a major contribution and is responsible for a substantially larger cross section (factor of 5 or so) as compared to $pp\gamma$.

The qualitative structure of the electric and magnetic contributions are readily understood from expansions of the scattering amplitude. For the electric part and solely for the $^1S_0$ channel, the scattering amplitude varies as $\boldsymbol{\varepsilon}\cdot\mathbf{Q}$, where [5]

$$\mathbf{Q} = \mathbf{K}'\left(\hat{\mathbf{k}}\cdot\mathbf{K}'\right) f_1(k,K',K) - \mathbf{K}\left(\hat{\mathbf{k}}\cdot\mathbf{K}\right) f_2(k,K',K) \tag{48}$$

involves the relative momenta of the two protons initially ($\mathbf{K}$) and finally ($\mathbf{K}'$) with f_1, f_2 being appropriate functions of the momenta, and the scalar product is taken with the polarization vector, $\boldsymbol{\varepsilon}$. Considering coplanar events, for simplicity, the scalar products vanish at $\theta_\gamma = 0$ and $180°$ while for $\theta_\gamma = 90°$ the amplitude is very small, as $\boldsymbol{\varepsilon}\cdot\mathbf{K}' \simeq 0$. Likewise, the isotropic nature of the magnetic cross sections can be anticipated since the Pauli spin operator, $\boldsymbol{\sigma}$, is independent of spatial coordinates and matrix elements are defined in the transverse gauge. There is little effect, then, with photon angle. The extreme photon angle enhancement observed for the forward proton angle, $(12°, 12°)$, cross sections is due to the phase space factor, which is essentially constant for the $(30°, 30°)$ kinematics.

The $(12°, 12°)$ noncoplanar cross sections in Fig. 7 show little change in features as a function of the noncoplanarity angle, $\bar{\phi}$, at 280 MeV. The electric contribution is small enough that no major structural changes due to $\bar{\phi}$ variation are observed. Wider proton opening angles are needed to observe in the cross section behavior effects of the known reduction of the electric part [5] as a function of $\bar{\phi}$. This is demonstrated in Fig. 13 wherein the 150 MeV cross sections are displayed on the left and the 280 MeV ones on the right, for the $(30°, 30°)$ case and symmetric azimuthal angles, $\bar{\phi}$, as labeled. For these energies $\bar{\phi} = 4.4°$ and $5.8°$, respectively, are the noncoplanar limits. Again, the electric, magnetic, and complete cross sections are displayed by the long-dashed, short-dashed, and continuous lines, respectively. The noncoplanar features generally look similar for both energies and, indeed, seem to be more sensitive to the proton opening angles than to energy. The noncoplanar geometry changes qualitatively the cross section, unlike any coplanar variation. The initial effect of noncoplanarity is to drop the cross section at forward and increase it at backward photon angles. It is the phase space factor that is largely responsible for this and for the changes in the magnetic contribution away from the isotropic coplanar result. The coplanar quadrupole shape of the electric contribution is slowly suppressed with increasing $\bar{\phi}$. The decrease in the total T-matrix amplitude leaves a reduced but finite result at the kinematic limit so that the cross section is basically featureless there. This is to be expected as all photon emissions approach the limiting photon with increasing angle, $\bar{\phi}$. At the limit we are essentially observing photon emissions of the same orientation.

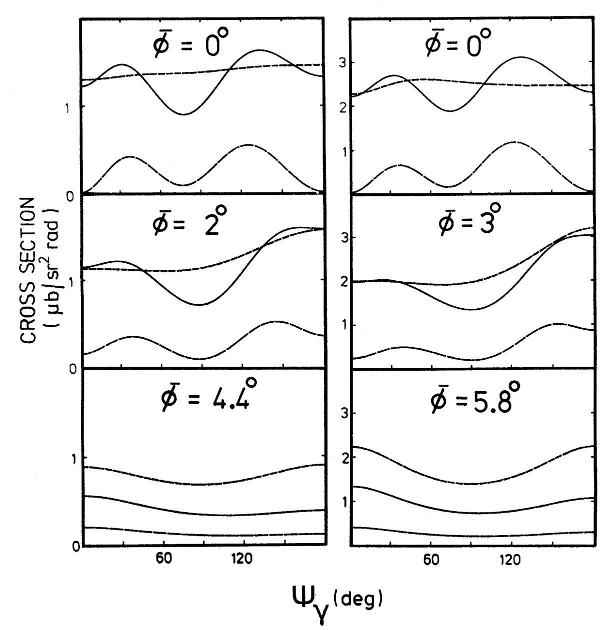

FIG. 13. Cross sections for $\bar{\theta} = 30°$ at 150 MeV (left panels) and 280 MeV (right panels) using the Paris interaction. Results are for the coplanar geometry (top panels), $\bar{\phi} = 2°$ (left middle panel) and $\bar{\phi} = 3°$ (right middle panel), and at the noncoplanar limit (bottom panels). The solid curve represents the full result. The long-dashed and short-dashed lines are for the electric and magnetic contributions, respectively.

F. Inclusion of higher partial waves and RSC

In any calculation, a choice must be made of a cutoff in the two-nucleon channel (J) contributions. That choice must yield sufficient convergence in calculations if results are to be meaningful. Various such truncations were used in calculations made in coplanar geometries for the $pp\gamma$ cross sections and the analyzing powers that are shown in Fig. 14. The Paris t matrices were used and the results calculated for $\bar{\theta} = 12°$ and for $\bar{\theta} = 30°$ are given on the left and right, respectively. The results for $J \leq 4$ are shown by the continuous lines and adding to that all $J = 5$ contributions yields the long-dashed curves. Including all t matrices for $J \leq 8$ gave the results that are displayed by the dot-dashed curves which are almost identical to results obtained using the Paris t matrices for $J \leq 6$. Also, calculations were made including higher partial waves ($J < 20$) approximated by an OPE interaction set of t matrices taken in the on-shell approximation in the same way as Workman and Fearing [1, 35]. For the $J \leq 6$ calculation the OPE amplitudes make very little difference to either cross section or analyzing powers. It is this latter prescription that is used for all results unless otherwise stated (note that the ERSC is calculated for $J \leq 5$ with OPE amplitudes for higher J channels). Clearly, few changes occur on inclusion of $J > 4$ channels, the largest being a 10% rise at backward photon angles for the $\theta = 30°$ cross section. Given the sensitivity of A_y to the tensor channels, almost all the information there is carried by the $J \leq 4$ channels.

The RSC have been included in all calculations, to $O(m^{-3})$. The effect of these corrections are shown in Fig. 15 for coplanar cross sections and analyzing powers (A_y) which are compared with the TRIUMF data [16] for the most extreme proton opening angles. The calculations with the RSC gave the results displayed by the continuous curves. Although they obviously grow in

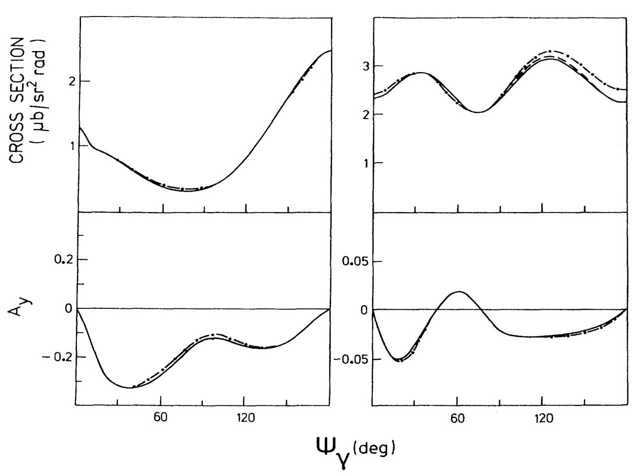

FIG. 14. Calculated coplanar cross section (upper panels) and A_y (lower panels) at 280 MeV for $\theta = 12°$ (left panels) and $\theta = 30°$ (right panels) geometries using the Paris interaction. The solid, dashed, and dot-dashed curves are for the calculations including only $J \leq 4$, $J \leq 5$, $J \leq 8$ partial waves.

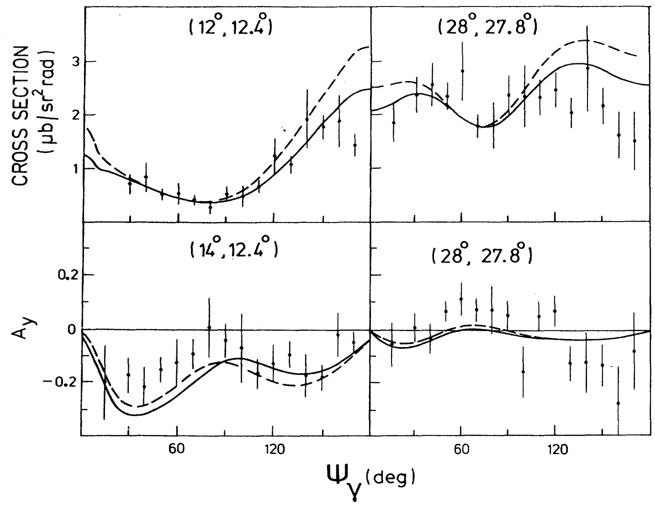

FIG. 15. Calculated coplanar cross section (upper panels) and A_y (lower panels) at 280 MeV for the geometries as shown, using the Paris interaction and compared with the TRIUMF data. The solid lines are for the full calculation and for the dashed lines the RSC are excluded.

importance with energy, to 15–20 % at 280 MeV, they always drop the cross section either side of the minimum. In comparison, the A_y results are less affected; particularly for the larger proton polar angle results. Indeed, the TRIUMF (A_y) data do not differentiate between the calculations with and without the corrections, although the cross section data, one might suggest, indicate a preference for the inclusion of these RSC. However, inclusion of the rescattering term [3] appears to have virtually the opposite effects qualitatively and quantitatively and, at the very least, will have some off-setting interference with the RSC. For completeness note that the TRIUMF data used here do not include the $\frac{2}{3}$ scaling suggested by Michaelian *et al.* [16].

VIII. CONCLUSIONS

Both coplanar and noncoplanar calculations of pp bremsstrahlung reveal that proper off-of-the-energy-shell t matrices must be used in analyses; especially for forward proton scattering (compared to the kinematic limit). The data at 280 MeV [cross sections and analyzing powers (A_y) in the coplanar geometry] do not distinguish between the off-shell properties of "realistic" interactions. That may always be the case since local interactions that fit the same on-shell data (phase shifts) have very similar off-energy-shell t matrices for the range of momenta corresponding to the bremsstrahlung kinematics.

Our results have shown sensitivity to components of the t matrices, notably the triplet P waves and the tensor coupled P-F channels. At 280 MeV the effects of the $^1S_0$ channel are not very significant. We note that all $J = 0$ and 1 channels contribute about a half of the cross sections but these may not necessarily be the dominant contributors off of the energy shell. Channels with $J > 6$ are negligible.

Azimuthal (noncoplanar) variation revealed that the 280 MeV cross section values at large photon angles (ψ_γ) vary most markedly. In contrast A_y gradually decreases until it vanishes at the kinematic limit. A_x and A_z have quite unique structures for noncoplanar geometries. The tensor coupled, ${}^3P_2$ -${}^3F_2$, and ${}^3P_0$ channel off-shell effects are most important in the results for A_x while the ${}^3P_0$ channel is crucial for A_z. Maximal effects at 280 MeV seem to occur for $\bar{\phi} \simeq 4°$.

The structure of the 280 MeV cross sections is dominated by magnetic contributions in all geometries. The changing integrated cross section shapes (with $\bar{\phi}$) reflect the variation in relative importance as well as of interference between convection and magnetization current expectations.

We gratefully acknowledge Martin Jetter and Professor Heinz von Geramb of the University of Hamburg for providing the opportunity to compare calculations and thus correct errors in our calculated results.

[1] R. L. Workman and H. W. Fearing, Phys. Rev. C **34**, 780 (1986).
[2] K. Nakayama, Phys. Rev. C **39**, 1475 (1989).
[3] V. R. Brown, P. L. Anthony, and J. Franklin, Phys. Rev. C **44**, 1296 (1991).
[4] B. v. Przewoski, H. O. Meyer, H. Nann, P. V. Pancella, S. F. Pate, R. E. Pollock, T. Rinckel, M. A. Ross, and F. Sperisen, Phys. Rev. C **45**, 2001 (1992).
[5] D. Drechsel and L. C. Maximon, Ann. Phys. **49**, 403 (1968).
[6] M. K. Liou and M. I. Sobel, Ann. Phys. **72**, 323 (1972).
[7] M. K. Liou and K. S. Cho, Nucl. Phys. **A124**, 85 (1969).
[8] M. Lacombe, B. Loiseau, J. M. Richard, R. Vinh Mau, J. Côté, P. Pirès, and R. de Tourreil, Phys. Rev. C **21**, 861 (1980).
[9] R. Machleidt, K. Holinde, and Ch. Elster, Phys. Rep. **149**, 1 (1987).
[10] B. D. Day, Phys. Rev. C **24**, 1213 (1981).
[11] L. Petris, J. Phys. G **7**, 309 (1981); L. Berge and L. Petris, Aust. J. Phys. **39**, 461 (1986).
[12] R. A. Arndt, L. D. Roper, R. A. Bryan, R. B. Clark, and B. J. VerWest, Phys. Rev. D **28**, 97 (1983); R. A. Arndt, J. S. Hyslop III, and L. D. Roper, *ibid.* **35**, 128 (1987).
[13] B. Gottschalk, W. J. Shlaer, and K. H. Wang, Nucl. Phys. **A94**, 491 (1967).
[14] V. Brown, Phys. Rev. **177**, 1498 (1969).
[15] L. Heller and M. Rich, Phys. Rev. C **10**, 479 (1974).
[16] K. Michaelian *et al.*, Phys. Rev. D **41**, 2689 (1990).
[17] P. Kitching *et al.*, Nucl. Phys. **A463**, 87c (1987).
[18] H. W. Fearing, Nucl. Phys. **A463**, 95c (1987).
[19] M. Gell-Mann and M. L. Goldberger, Phys. Rev. **91**, 398 (1953).
[20] A. H. Cromer and M. I. Sobel, Phys. Rev. **152**, 1351 (1966); L. Wolfenstein and J. Ashkin, *ibid.* **85**, 947 (1952).
[21] F. E. Low, Phys. Rev. **110**, 974 (1958); E. M. Nyman, *ibid.* **170**, 1628 (1969); H. W. Fearing, Phys. Rev. C **6**, 1136 (1972); Phys. Rev. Lett. **42**, 1394 (1979); Phys. Rev. C **22**, 1388 (1980).
[22] L. Heller, Phys. Rev. **174**, 1580 (1968).
[23] V. Herrmann, J. Speth, and K. Nakayama, Phys. Rev. C **43**, 394 (1991).
[24] V. R. Brown, Phys. Lett. **25B**, 506 (1967).
[25] L. L. Foldy and S. A. Wouthuysen, Phys. Rev. **78**, 29 (1950).
[26] R. A. Krajcik and L. L. Foldy, Phys. Rev. Lett. **24**, 545 (1970); F. E. Close and L. A. Copley, Nucl. Phys. **B19**, 477 (1970).
[27] H. P. Noyes, Phys. Rev. Lett. **15**, 538 (1965); K. L. Kowalski, *ibid.* **15**, 798 (1965).
[28] K. Amos, L. Berge, F. A. Brieva, A. Katsogiannis, L. Petris, and L. Rikus, Phys. Rev. C **37**, 934 (1988).
[29] H. P. Stapp, T. J. Ypsilantis, and N. Metropolis, Phys. Rev. **105**, 302 (1957).
[30] D. A. Varshalovich, A. N. Moskalev, and V. K. Khersonskii, *Quantum Theory of Angular Momentum* (World Scientific, New Jersey, 1988).
[31] E. U. Condon and Q. W. Shortley, *The Theory of Atomic Spectra* (Cambridge University Press, Cambridge, 1935).
[32] M. L. Goldberger and K. M. Watson, *Collision Theory* (Wiley, New York, 1964), pp. 384 and 385.
[33] M. Haftel and F. Tabakin, Nucl. Phys. **A158**, 1 (1970).
[34] W. H. Press, B. P. Flannery, S. A. Teukolsky, and W. T. Vetterling, *Numerical Recipes* (Cambridge University Press, Cambridge, 1986), Chap. 2.
[35] P. Cziffra, M. H. MacGregor, M. J. Moravcsik, and H. P. Stapp, Phys. Rev. **114**, 880 (1959).
[36] Y. Ueda, Phys. Rev. **145**, 1214 (1966).
[37] H. von Geramb and M. Jetter, University of Hamburg, private communication.
[38] M. E. Rose, *Elementary Theory of Angular Momentum* (Wiley, New York, 1957), Chap. 4.
[39] H. Goldstein, *Classical Mechanics* (Addison-Wesley, Reading, Massachusetts, 1980), Chap. 4.
[40] V. Herrmann and K. Nakayama, Phys. Rev. C **45**, 1450 (1992); V. Herrmann and K. Nakayama, IKP Annual Report, 1990, p. 90.
[41] H. W. Fearing, TRIUMF, private communication.
[42] V. Herrmann and K. Nakayama, IKP Annual Report, 1990, p. 87; IKP Annual Report, 1989, p. 136.